Available online at www.sciencedirect.com

SCIENCE DIRECT

International Journal of Heat and Fluid Flow 27 (2006) 371–390

International Journal of HEAT AND FLUID FLOW

www.elsevier.com/locate/ijhff

Large eddy simulation of turbulent heat transfer in a rotating square duct

Zhaohui Qin [a], Richard H. Pletcher [b,*]

[a] *Department of Mechanical Engineering, 2025 Black Engineering Building, Iowa State University, Ames, IA 50011, USA*
[b] *Department of Mechanical Engineering, 3024 Black Engineering Building, Iowa State University, Ames, IA 50011, USA*

Received 26 July 2005; accepted 11 January 2006
Available online 7 March 2006

Abstract

Large eddy simulations of turbulent mixed convection heat transfer in a variable-property thermally developing rotating square duct are presented. A finite volume lower–upper symmetric Gauss–Seidel (LU-SGS) scheme coupled with time derivative preconditioning is used to simulate low Mach number compressible three-dimensional turbulent flow. A localized dynamic subgrid-scale (SGS) model is used to evaluate the unresolved stresses. Characteristic outflow conditions are employed so that the flow can develop further as it responds to the heating as well as rotating conditions. Several isothermal rotating duct cases were calculated and compared with previous DNS results to validate the numerical procedure. Then heated rotating ducts under constant wall heat flux are simulated. The wall heat flux is strong enough to cause the flow to separate in the outward mixed convections. A vanishing inviscid flux derivative method is designed to overcome the difficulty caused by the velocity reversal at the duct outlet when the flow separates. The Reynolds number varies from 4500 to 10,000; The rotation number changes from 0.0133 to 0.176; The Grashof number ranges from -2.2×10^6 to 2.2×10^6. Simulation of forced and mixed convection cases shows that the flow is strongly influenced by the Coriolis and centrifugal buoyancy forces through complex and delicate mechanisms.

PACS: 44.15.+a; 47.27.Eq; 47.27.Te; 47.32.−y

Keywords: Large eddy simulation; Turbulent heat transfer; Rotating square duct; Developing flow; Mixed convection

---

1. Introduction

Turbulent flow and related heat transfer inside a square duct rotating about an axis perpendicular to one of the walls has many engineering applications such as internal cooling of turbine blades and automobile brakes. One of the primary concerns in these applications is the heat transfer coefficients on each wall of the rotating passage when the fluid inside is thermally developing. In turbulent duct flows, it is well known that Prandtl's secondary flow of the second kind has a significant effect on the transport of heat and momentum. This secondary flow causes distortion of the isolines of mean velocity, temperature, and their fluctuations. With rotation, Coriolis and centrifugal buoyancy forces change the mean velocity profile as well as cause a more complicated secondary flow pattern and, as a consequence, modify the heat transfer coefficient distributions on each wall.

Due to its value in military and commercial applications, the theoretical research on rotating duct flows can be traced back as far as to the 1970s. Smirnov (1978) obtained an asymptotic solution of the laminar rotating duct and gave a drag formula for this situation. Ovchinnikov and Rukolaine (1985) studied the development of laminar flow in a prismatic duct uniformly rotating about the

---

* Corresponding author. Tel.: +1 515 294 2656; fax: +1 515 294 3261.
E-mail address: pletcher@iastate.edu (R.H. Pletcher).

0142-727X/$ - see front matter © 2006 Elsevier Inc. All rights reserved.
doi:10.1016/j.ijheatfluidflow.2006.01.003

Nomenclature

C_d	dynamic subgrid-scale model coefficient
D_h	hydraulic diameter
$\mathscr{F}$	the inviscid part of flux $\mathbf{F}$
$\mathbf{F}$	vector of fluxes
G	turbulent production caused by rotation
G_Δ	filter function
Gr	Grashof number
$\mathscr{L}$	amplitude variation of characteristic wave
L	length
M	total turbulent production
Nu	Nusselt number
P	turbulent production caused by mean shear
Pr	Prandtl number
Pr_t	turbulent Prandtl number
R	gas constant
Re	Reynolds number
Ro	rotation number
$\widetilde{S}_{ij}$	strain rate tensor
T	temperature or Jacobian matrix
T_τ	friction temperature
U	velocity
$\mathbf{U}$	vector of conserved variables
$\mathbf{W}$	vector of primitive variables
c	sound speed
c_p	constant pressure specific heat
c_v	constant volume specific heat
$\hat{e}$	resolved total energy
f	forcing function or friction factor
h	half D_h or heat transfer coefficient
k	thermal conductivity or turbulent kinetic energy
$\bar{p}$	thermodynamic pressure
$\hat{q}_i$	heat flux vector
q_{ti}	heat flux vector
u	velocity or streamwise velocity
u_τ	friction velocity
β	volumetric expansion coefficient
γ	ratio of specific heats
δ	distance or Kronecker delta
θ	temperature difference
μ	molecular dynamic viscosity
μ_t	subgrid-scale turbulent viscosity
ν	kinematic viscosity
ρ	density
$\hat{\sigma}_{ij}$	viscous stress tensor
Ω	control volume
τ_{ij}	subgrid-scale stress tensor
Δ	filter width
$\hat{\Delta}$	test filter width

Subscripts

b	bulk property
loc	local value
r	reference variables
rms	root mean square
s	stationary duct value
w	wall value

Superscripts and other symbols

$+$	wall coordinates
★	dimensional variables
$'$	fluctuation
$\bar{\ }$	resolved or large scale component of filtered quantity
$\tilde{\ }$	resolved or large scale component of Favre filtered quantity
$\hat{\ }$	test filtered quantity
m	index for pseudo time step

Abbreviations

DNS	direct numerical simulation
LES	large eddy simulation
LU-SGS	lower–upper symmetric Gauss–Seidel
NSCBC	Navier–Stokes characteristic boundary conditions
RANS	Reynolds-averaged Navier–Stokes
SGS	subgrid-scale
TKE	turbulent kinetic energy

transverse axis. Although extensive experiments (Wagner et al., 1991; Morris and Ghavami-Nasr, 1991; Han and Zhang, 1992; Han et al., 1993; Macfarlane and Joubert, 1998; Liou et al., 2001, 2003; Martensson et al., 2002) and numerical studies based on the Reynolds-averaged Navier–Stokes (RANS) equations (Prakash and Zerkle, 1992; Tekriwal, 1994; Dutta et al., 1996; Hwang et al., 1998; Lin et al., 2001; Belhoucine et al., 2004) have been carried out on this topic, relatively few direct numerical simulations (DNS) or large eddy simulations (LES) results are available, especially results in which property variations are taken into account. Kristoffersen and Andersson did direct simulations of low Reynolds number turbulent flow in a rotating channel (Kristoffersen and Andersson, 1993). Tafti and Vanka carried out large eddy simulations of rotating turbulent channel flow (Tafti and Vanka, 1991). Simulation of isothermal rotating ducts by Gavrilakis (private communication) is the only available DNS result for rotating ducts according to the authors' knowledge. Pallares and Davidson (2000, 2002) did LES of turbulent heat transfer in both stationary and rotating square ducts. Murata et al. did large eddy simulations of turbulent heat transfer in rotating ducts with and without ribs (Murata and Mochizuki, 1999, 2001, 2004). Most of these recent papers used the incompressible Navier–Stokes equations and periodic boundary conditions for streamwise velocity and temperature because the fully developed region was their main concern. A good review on rotating internal flows without heat transfer can be found in Chapter 7 of Greitzer et al. (2004).

The previous researches provided much insight into the nature of the turbulent heat transfer in a fully developed rotating duct. However, a full appreciation of this phenomenon would require a more complete understanding of the details of the fluid motion. This led to the initiation of the current effort to simulate hydrodynamically developed turbulent air flow thermally developing in a four-heated-wall rotating square duct at low Mach number using large eddy simulation. The objective of this study is to develop an LES procedure to correctly predict complex turbulent flow phenomena with heat transfer and property variations and to obtain a better understanding of the physics of turbulent flow under rotating conditions. This study analyzes the air flow thermally developing in an orthogonally rotating straight smooth square duct at different Reynolds and rotation numbers. The centrifugal buoyancy effect is examined by varying the Grashof number. The constant wall heat flux condition is used in the present research. A finite volume LU-SGS scheme coupled with time derivative preconditioning is employed to solve the three-dimensional low Mach number compressible Navier–Stokes equations. Characteristic outflow boundary conditions are applied so that the flow can develop further as it responds to heating and rotating conditions. This method has been successfully implemented in the study of turbulent heat transfer in a stationary square duct (Qin and Pletcher, 2004) and LES of supercritical CO_2 pipe flow with constant wall heat flux (Wang and Pletcher, 2005). A vanishing inviscid flux derivative method is designed to avoid the possible difficulty caused by velocity reversal at the outlet which may occur as a result of an opposing centrifugal buoyancy force. To verify the code, we calculate several isothermal rotating duct cases and compare our results with DNS results. Then heated duct flow cases are simulated and the results are compared with available numerical and experimental data.

The rest of this paper is organized in two sections: the governing equations and the numerical method are described in the following section which is followed by the presentation and discussion of results.

2. Governing equations and numerical scheme

2.1. Governing equations

For gas flows with property variations, the compressible Navier–Stokes equations are applicable even if a low Mach number case is treated. The governing equations for large eddy simulation are obtained by filtering the non-dimensional compressible Navier–Stokes equations in a Cartesian coordinate system. In the current research, the top-hat filter is used and Favre averaging is employed to simplify the filtered equations. The resulting equations can be written in vector form as

$$\frac{\partial \bar{\mathbf{U}}}{\partial t} + \frac{\partial \bar{\mathbf{F}}_i}{\partial x_i} = \bar{\mathbf{S}}, \tag{1}$$

where

$$\bar{\mathbf{U}} = (\bar{\rho}, \bar{\rho}\tilde{u}, \bar{\rho}\tilde{v}, \bar{\rho}\tilde{w}, \bar{\rho}\tilde{e})^{\mathrm{T}}. \tag{2}$$

The total energy

$$\hat{e} = c_v\tilde{T} + \frac{1}{2}\tilde{u}_i\tilde{u}_i. \tag{3}$$

The resolved fluxes $\bar{\mathbf{F}}_i$ are

$$\bar{\mathbf{F}}_i = \begin{pmatrix} \bar{\rho}\tilde{u}_i \\ \bar{\rho}\tilde{u}_i\tilde{u}_1 - \hat{\sigma}_{i1} + \tau_{i1} \\ \bar{\rho}\tilde{u}_i\tilde{u}_2 - \hat{\sigma}_{i2} + \tau_{i2} \\ \bar{\rho}\tilde{u}_i\tilde{u}_3 - \hat{\sigma}_{i3} + \tau_{i3} \\ \bar{\rho}\hat{e}\tilde{u}_i - \tilde{u}_j\hat{\sigma}_{ij} + \hat{q}_i + q_{ti} \end{pmatrix}, \tag{4}$$

where the stress tensor is

$$\hat{\sigma}_{ij} = -\bar{p}\delta_{ij} + \frac{2\tilde{\mu}}{Re_{\mathrm{r}}}\left(\bar{S}_{ij} - \frac{1}{3}\bar{S}_{kk}\delta_{ij}\right) \tag{5}$$

and $\bar{S}_{ij}$ is the strain rate tensor which is

$$\bar{S}_{ij} = \frac{1}{2}\left(\frac{\partial \tilde{u}_i}{\partial x_j} + \frac{\partial \tilde{u}_j}{\partial x_i}\right). \tag{6}$$

The heat flux vector is given by Fourier's law

$$\hat{q}_i = -\frac{c_p\tilde{\mu}}{Re_{\mathrm{r}}Pr}\frac{\partial \widetilde{T}}{\partial x_i}. \tag{7}$$

The subgrid-scale stress is

$$\tau_{ij} = \bar{\rho}(\widetilde{u_iu_j} - \tilde{u}_i\tilde{u}_j), \tag{8}$$

and the subgrid-scale heat flux is

$$q_{ti} = \bar{\rho}c_v(\widetilde{Tu_i} - \tilde{T}\tilde{u}_i). \tag{9}$$

$\bar{\mathbf{S}}$ is the resolved source term including any possible body forces. Under a rotating frame, the flow will feel both Coriolis forces and a centrifugal buoyancy force. When the rotation is in the z direction and the x coordinate is aligned with the flow direction as Fig. 1 shows, the source term becomes

$$\mathbf{S} = \left(0, 2\bar{\rho}Ro\tilde{u}_2 + \frac{Gr}{\eta Re_{\mathrm{r}}^2}\bar{\rho}, -2\bar{\rho}Ro\tilde{u}_1, 0, -\alpha - \pi - \varepsilon\right)^{\mathrm{T}}, \tag{10}$$

where the Reynolds number, rotation number Ro and Grashof number Gr are defined as

$$Re_{\mathrm{r}} = \frac{\rho_{\mathrm{r}}V_{\mathrm{r}}L_{\mathrm{r}}}{\mu_{\mathrm{r}}}, \quad Ro = \frac{\omega L_{\mathrm{r}}}{V_{\mathrm{r}}},$$

$$Gr = \frac{\rho_{\mathrm{r}}^2\beta(T_{\mathrm{w}} - T_{\mathrm{r}})\omega^2 r_{\mathrm{m}}L_{\mathrm{r}}^3}{\mu_{\mathrm{r}}^2}, \tag{11}$$

in which r_{m} is the mean rotating radius, ω the angular velocity and $\eta = \beta(T_{\mathrm{w}} - T_{\mathrm{r}})$. Two situations, namely

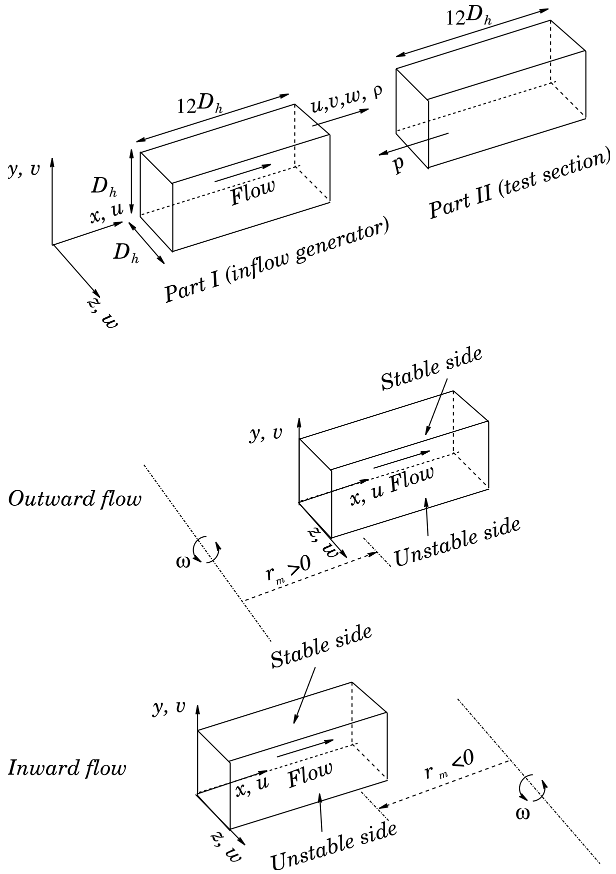

Fig. 1. Sketch of the computational domain.

outward flows and inward flows, are studied for the heated duct cases (see Fig. 1). For the outward flows, fluid flows away from the rotation axis and the Grashof number is positive. Since the flow is in the same direction as the centrifugal force, buoyancy acts against the high temperature fluid flow (opposing buoyancy); for the inward flows, on the contrary, fluid flows toward the rotation axis and the Grashof number is negative. Since the flow is in the opposite direction to that of the centrifugal force, buoyancy aids the high temperature fluid flow (aiding buoyancy). The last three terms in the source term are

$$\alpha = \tilde{u}_j \frac{\partial \tau_{ij}}{\partial x_i}, \quad \pi = \overline{p \frac{\partial u_i}{\partial x_i}} - \bar{p}\frac{\tilde{u}_i}{x_i}, \quad \varepsilon = \overline{\sigma_{ij}\frac{\partial u_j}{\partial x_i}} - \bar{\sigma}_{ij}\frac{\partial \tilde{u}_j}{\partial x_i}. \tag{12}$$

For the present work, α, π and ε are neglected because of the low Mach number (0.001) used (Vreman et al., 1995).

For an ideal gas, the equation of state is

$$\bar{p} = \bar{\rho} R \tilde{T}, \tag{13}$$

and the molecular viscosity is evaluated by the power law

$$\mu = T^{0.71}. \tag{14}$$

The non-dimensional variables are defined as follows:

$$\begin{aligned}
&x_i = \frac{x_i^\star}{L_\mathrm{r}}, \quad t = \frac{t^\star}{L_\mathrm{r}/V_\mathrm{r}}, \quad u_i = \frac{u_i^\star}{V_\mathrm{r}}, \\
&p = \frac{p^\star}{\rho_\mathrm{r} V_\mathrm{r}^2}, \quad \rho = \frac{\rho^\star}{\rho_\mathrm{r}}, \quad T = \frac{T^\star}{T_\mathrm{r}}, \\
&e = \frac{e^\star}{V_\mathrm{r}^2}, \quad R = \frac{R^\star}{V_\mathrm{r}^2/T_\mathrm{r}}, \quad c_p = \frac{c_p^\star}{V_\mathrm{r}^2/T_\mathrm{r}}, \\
&\mu = \frac{\mu^\star}{\mu_\mathrm{r}}, \quad c_v = \frac{c_v^\star}{V_\mathrm{r}^2/T_\mathrm{r}},
\end{aligned} \tag{15}$$

in which dimensional variables are denoted with a superscript asterisk and the subscript r denotes reference values. M_r, L_r, V_r, ρ_r, T_r and μ_r are inflow Mach number, hydraulic diameter of the duct, inflow mean velocity, inflow mean density, inflow mean temperature and molecular viscosity evaluated by inflow mean temperature, respectively.

2.2. Subgrid-scale modeling

The above system can be closed by modeling the subgrid-scale stress and heat flux. The localized dynamic model proposed by Piomelli and Liu (1995) is used to evaluate the subgrid-scale stress terms. The turbulent heat flux is modeled following Wang and Pletcher (1996).

2.3. Numerical scheme

The governing equations are solved with a coupled finite volume method (Qin and Pletcher, 2004). Time derivative preconditioning developed by Pletcher and Chen (1993) is adopted to overcome the singularity caused by low Mach number. This preconditioning introduces a pseudo temporal derivative into the equation. Then the preconditioned time accurate governing equation is solved by the lower–upper symmetric Gauss–Seidel (LU-SGS) scheme (Rieger and Jameson, 1988) in a dual time-stepping approach.

2.4. Outflow boundary treatment

To let the flow develop thermally, the whole computational domain is separated into two parts, as shown in Fig. 1. Spatially periodic boundary conditions are applied to the first (or, the inflow generator) part of the domain to generate a realistic fully developed turbulent inflow field for the second (or, the test section) part. The pressure at the test section entrance is extrapolated from the interior of the domain, however. To ensure that the mass flow rate of the two parts are the same, the temperature at the entrance of the test section is recalculated according to the extrapolated pressure so that the density is unchanged across the entrance section. In the inflow generator, since a periodic boundary is used, a forcing function $f(t)$ is employed in the streamwise momentum equation to maintain a constant targeted mass flow rate. This forcing function term has been widely used in numerical simulations (see e.g. (Wang and Pletcher, 1996)). Such a forcing function is not needed in the test section.

At the outlet of the test section, Navier–Stokes characteristic boundary conditions (NSCBC) are applied. This method, which intends to provide time-accurate boundary conditions, was proposed by Thompson (1987, 1990) and then was further developed by Poinsot and Lele (1992) and Kim and Lee (2000, 2004). This method is incorporated into the LU-SGS solver as follows.

After dropping all filtering symbols, Eq. (1) can be recast in terms of primitive variables as

$$[T]\frac{\partial \mathbf{W}}{\partial t}+\frac{\partial \mathbf{F}_i}{\partial x_i}=\mathbf{S}, \tag{16}$$

where $\mathbf{W}=(p,u,v,w,T)^{\mathrm{T}}$ and $[T]=\frac{\partial \mathbf{U}}{\partial \mathbf{W}}$ is the Jacobian matrix. The flux term $\mathbf{F}_i$ can be decomposed into two parts: the inviscid part $\mathscr{F}_i$ and another part $\mathbb{F}_i$, which takes care of the viscous and subgrid-scale terms. Consider the characteristic form of Eq. (16) in the x_1 direction (since the normal to the outlet is in the x_1 direction in the present work):

$$[T]\frac{\partial \mathbf{W}}{\partial t}+\frac{\partial \mathscr{F}_1}{\partial x_1}+\mathbb{C}=\mathbf{0}, \tag{17}$$

where $\mathbb{C}$ is the combination of the source term and flux derivative terms excluding $\frac{\partial \mathscr{F}_1}{\partial x_1}$. Define $[A]_i=\frac{\partial \mathscr{F}_i}{\partial \mathbf{W}}$, $[\mathscr{A}]=[T]^{-1}[A]_1$ and $[\Lambda]=[S]^{-1}[\mathscr{A}][S]$, where $[\Lambda]$ is the diagonal matrix whose elements are eigenvalues of $[\mathscr{A}]$, and the rows of $[S]^{-1}$ are left eigenvectors. For an ideal gas, the five eigenvalues of $[\mathscr{A}]$ are $(u_1+c,u_1-c,u_1,u_1,u_1)$ where c is the local sound speed. Then Eq. (17) can be written as

$$[S]^{-1}\frac{\partial \mathbf{W}}{\partial t}+\underbrace{\overbrace{[\Lambda][S]^{-1}}^{[\Pi]}\frac{\partial \mathbf{W}}{\partial x_1}}_{\mathscr{L}}+[S]^{-1}[T]^{-1}\mathbb{C}=\mathbf{0}. \tag{18}$$

By employing the characteristic form, waves with different velocities can be determined separately. At the outflow boundary, waves leaving the domain are calculated using interior points and one-sided differences. Waves propagating into the domain, however, should be estimated by available information outside the domain and also by examination of the above equation. In the current simulation, if no heating is added, $u_1>0$ holds for all control volumes and $\mathscr{L}_2$ is the only incoming wave since its speed is negative (u_1-c). However, if heating is added and $Gr>0$, the opposing buoyancy force may cause the flow to separate and then the streamwise velocity becomes negative. Thus, there will be four rather than one incoming waves that need to be determined. To avoid such a situation, one can add an insulated buffer zone to the exit so that the separated region is eliminated. In the present study, instead of appending a buffer zone and then applying characteristic boundary conditions, a vanishing inviscid flux derivative method is designed for the outlet regions where $u_1<0$:

$$\frac{\partial \mathscr{F}_1}{\partial x_1}=0. \tag{19}$$

By multiplying by $[S]$, Eq. (18) becomes

$$\frac{\partial \mathbf{W}}{\partial t}+[S]\mathscr{L}+[T]^{-1}\mathbb{C}=\mathbf{0}. \tag{20}$$

A constant pressure at infinity is used as the outlet boundary condition in the present work. This is a partially reflecting condition. From Eq. (20), by neglecting the source, transverse and viscous terms, which is also called the local one-dimensional inviscid (LODI) assumption, we have

$$\frac{\partial p}{\partial t}+\frac{\gamma}{\gamma-1}\rho(\mathscr{L}_1+\mathscr{L}_2)=0. \tag{21}$$

Let $\frac{\partial p}{\partial t}=0$, then

$$\mathscr{L}_2=-\mathscr{L}_1. \tag{22}$$

To take into account of the effect of pressure at infinity, Eq. (22) is modified (Poinsot and Lele, 1992) as

$$\mathscr{L}_2=-\mathscr{L}_1+K(p-p_\infty), \tag{23}$$

where K is a positive constant (Rudy and Strikwerda, 1981). Since $\mathscr{L}=[\Pi]\frac{\partial \mathbf{W}}{\partial x_1}$, the matrix $[\Pi]$ is changed into $[\Pi]'$ according to Eq. (22). The waves at the outlet boundary thus become

$$\mathscr{L}=[\Pi]'\frac{\partial \mathbf{W}}{\partial x_1}+\mathbf{b}, \tag{24}$$

where $\mathbf{b}=(0,K(p-p_\infty),0,0,0)^{\mathrm{T}}$ And Eq. (18) becomes

$$[S]^{-1}\frac{\partial \mathbf{W}}{\partial t}+[\Pi]'\frac{\partial \mathbf{W}}{\partial x_1}+\mathbf{b}+[S]^{-1}[T]^{-1}\mathbb{C}=\mathbf{0}. \tag{25}$$

Multiplying by $[T][S]$, Eq. (25) becomes

$$[T]\frac{\partial \mathbf{W}}{\partial t}+[A]'_1\frac{\partial \mathbf{W}}{\partial x_1}+\mathbb{C}'=\mathbf{0}, \tag{26}$$

or

$$[T]\frac{\partial \mathbf{W}}{\partial t}+\frac{\partial \mathscr{F}'_1}{\partial x_1}+\mathbb{C}'=\mathbf{0}, \tag{27}$$

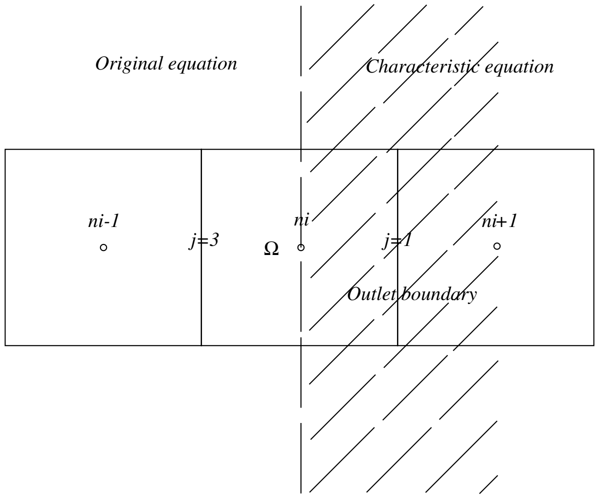

Fig. 2. Sketch of the outlet boundary.

where $[A]'_1 = [T][S][\Pi]'$, $\mathbb{C}' = \mathbb{C} + [T][S]\mathbf{b}$. Eq. (27) is of the same form of Eq. (17) and should be applied at the outlet surface as Fig. 2 indicates. At the outlet control volume *ni*, the x_1 direction flux derivative term should be evaluated according to Eq. (17) at face $j = 3$ (interior face) and according to Eq. (27) at face $j = 1$ (outlet boundary face), respectively. Note that $\mathscr{F}'_1$ is unknown (though we do know $\frac{\partial \mathscr{F}'_1}{\partial x_1}$ and $\frac{\partial \mathscr{F}'_1}{\partial \mathbf{W}}$, which is $[A]'_1$), thus, we evaluate the integral of the x_1 direction flux derivative term through the boundary control volume *ni* as

$$\begin{aligned}\int_\Omega \frac{\partial \mathbf{F}_1}{\partial x_1} \mathrm{d}\Omega \approx & \left(\mathbf{F}_{1ni}^{(m)} - \mathbf{F}_{13}^{(m)}\right) S_{13} \\ & + [([A]_1 \Delta\mathbf{W})_{ni} - ([A]_1 \Delta\mathbf{W})_3] S_{13} \\ & + \frac{\partial {\mathscr{F}'_1}^{(m)}}{\partial x_1} \frac{\Omega}{2} + [([A]'_1 \Delta\mathbf{W})_1 - ([A]'_1 \Delta\mathbf{W})_{ni}] S_{13},\end{aligned} \tag{28}$$

where S_{13} is the area of face $j = 1$ and $j = 3$. The subscript *ni* means the value at the center of control volume *ni*. For the preconditioned system, the process is essentially the same except that the eigenvalues of the matrix change. In the current LU-SGS scheme, the unsymmetry of equations used at different surfaces of the outlet control volume will cause the diagonal matrix in the $L - D - U$ decomposition to be no longer exactly diagonal. However, this difficulty can be removed by moving the non-diagonal elements to the corresponding locations in the lower and upper matrices.

3. Results and discussion

3.1. The isothermal duct

Several fully developed isothermal rotating duct cases (cases 1–4) were simulated. For these cases, step periodic boundary conditions were used. Cases 1 and 2 are compared with DNS results (Gavrilakis, private communication). The computational domain is shown in Fig. 1. A 240 × 40 × 40 grid was used for all computations. The grids were stretched toward the duct walls by using a hyperbolic tangent function (see Fig. 3). The effect of the grid spacing on the computed result was checked by increasing the grid number to 240 × 60 × 60 for cases 1 and 2, and no major differences have been observed (see Figs. 5, 6 and 10). The Mach number was 0.001 and the non-dimensional physical time step was 8.0×10^{-3}. The computational details are in Table 1.

Fig. 4 shows the mean velocity fields (only half the fields are shown since symmetry is taken into account). A main feature is the persistent secondary flows which are constituted by two counter-rotating cells (in half the cross section). The centers of the larger cells are close to the stable wall and their location moves to the corner as rotation number increases. The smaller cells are near the unstable wall and under the corner bisectors. The strength and size of the smaller cells increase when rotation number is increased. The generation of the big cell can be attributed to the balance between pressure gradient and the Coriolis force. At the center of the duct ($z/D_\mathrm{h} = 0.5$), the Coriolis force in the y direction is balanced by the pressure gradient. At the side walls ($z/D_\mathrm{h} = 0$ and 1), an Ekman layer is formed since the Coriolis force is reduced as streamwise velocity decreases and the pressure gradient in the y direction drives fluid so that it is balanced by both the Coriolis force and the viscous force.

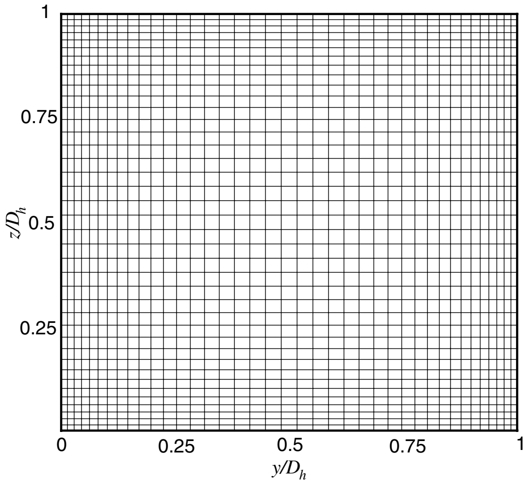

Fig. 3. A stretched grid.

Table 1
Computational details

Case	Re	Ro	q_w	$T_\mathrm{w}/T_\mathrm{b}$	Gr
1	4500	0.0133	0.0	1.0	0.0
2	4500	0.0266	0.0	1.0	0.0
3	5000	0.088	0.0	1.0	0.0
4	5000	0.176	0.0	1.0	0.0
5	5000	0.176	6.4×10^{-4}	–	0.0
6	5000	0.176	6.4×10^{-4}	–	1.1×10^{6}
7	5000	0.176	6.4×10^{-4}	–	2.2×10^{6}
8	5000	0.176	6.4×10^{-4}	–	-1.1×10^{6}
9	5000	0.176	6.4×10^{-4}	–	-2.2×10^{6}
10	5000	0.088	6.4×10^{-4}	–	2.2×10^{6}
11	10,000	0.088	1.1×10^{-3}	–	2.2×10^{6}

Though somewhat different from the ordinary concept of Ekman boundary layer which gives a spiral velocity variation, the Ekman layer in the current scenario is caused by the same force balance and has the same thickness as those of the traditional Ekman layer.

At the stable wall ($y/D_\mathrm{h} = 1$), a Stewartson layer (Stewartson, 1957) comes into being to transport mass flux from the Ekman layer to the interior flow. At the unstable wall ($y/D_\mathrm{h} = 0$), secondary flow of the second kind dominates since turbulence is enhanced there.

The secondary flow convection shifts the peak value of axial velocity toward the unstable wall which results in an almost linear velocity region (see Fig. 5). The range of the linear velocity region increases with higher rotation

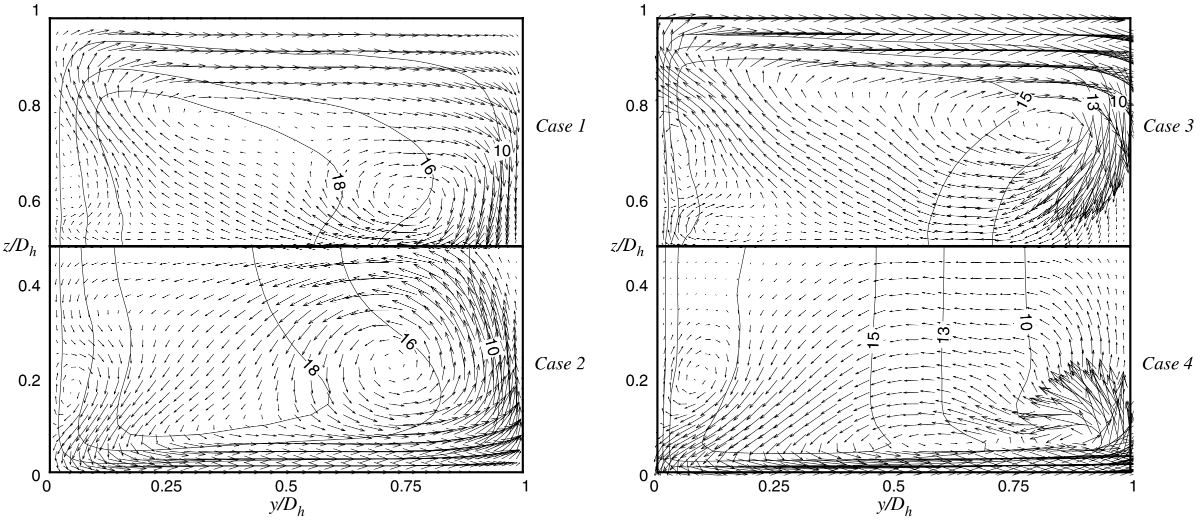

Fig. 4. Contours of the streamwise mean velocity together with the secondary flow vector field.

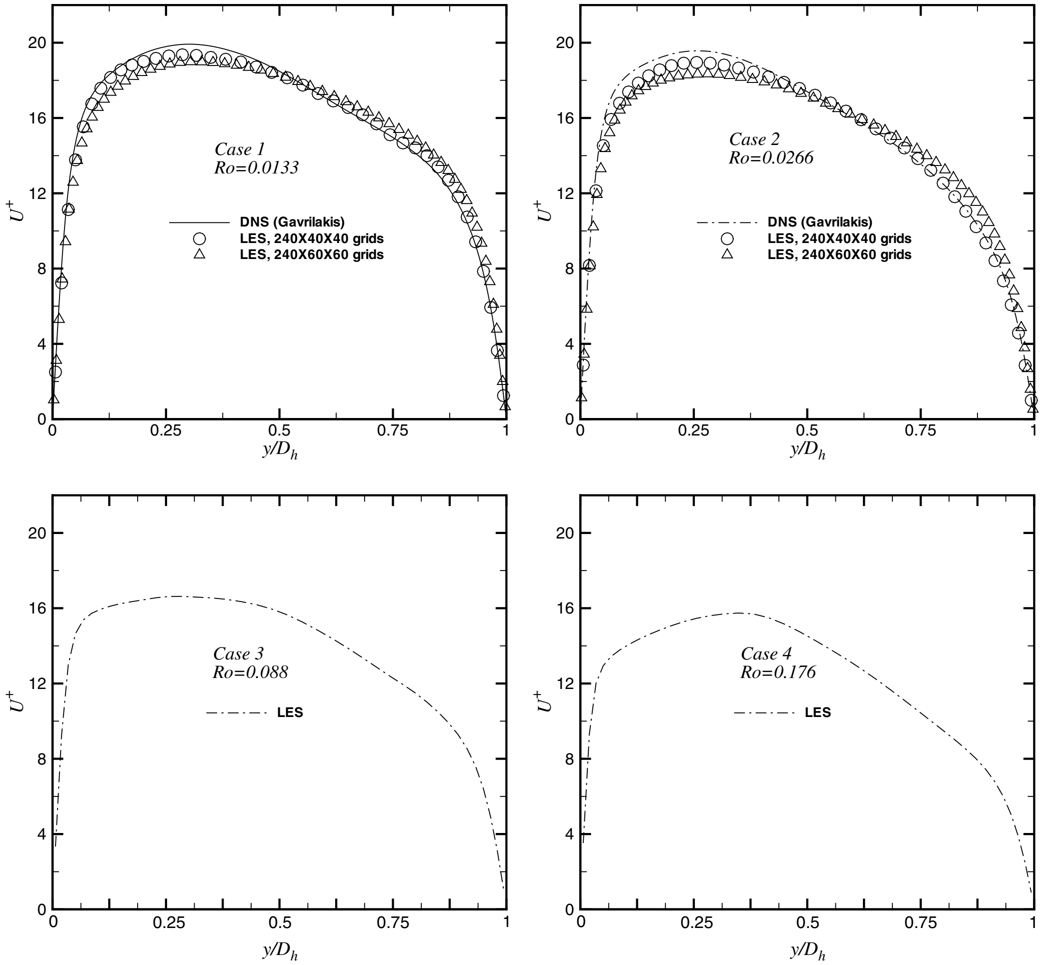

Fig. 5. Streamwise mean velocity along wall bisector $z/D_h = 0.5$.

number. The slope of the velocity profile, however, seems insensitive to the rotation rate. This can be compared with rotating turbulent channel flows, in which a linear velocity profile also shows up, however, its slope is $2Ro$ and its peak shifts toward the stable wall. When rotation rate increases, the Taylor–Proudman regime develops. That is, the interior flow field becomes uniform in the z direction (see case 4 in Fig. 4). This phenomenon is a result of the balance between

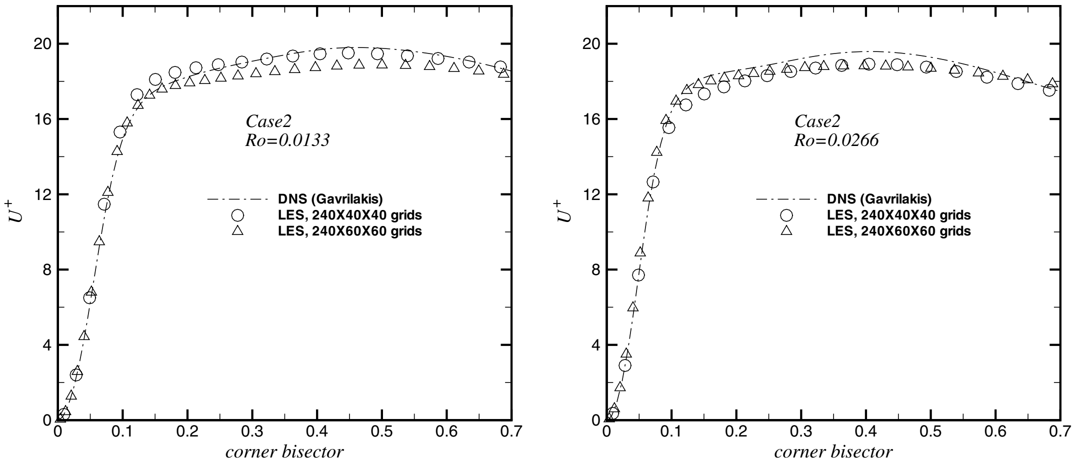

Fig. 6. Streamwise mean velocity along corner bisector.

pressure gradient and Coriolis force, which has no component in the z direction.

Fig. 5 shows the streamwise mean velocity profiles along the wall bisector $z/D_h = 0.5$ and Fig. 6 shows the streamwise mean velocity profiles along the corner bisector near the unstable wall. The mean velocity is normalized by the global wall friction velocity. The results are compared with DNS results (Gavrilakis, private communication). Very good agreement has been obtained. Fig. 7 compares the streamwise mean velocity profiles obtained for two rotating cases with that for a non-rotating case in wall coordinates. The inner variables U^+ and y^+ are based on the local friction velocities. The laminarization of turbulence on the stable side can be observed from the increased slope in the log-law region. On the unstable side, the enhanced turbulence causes a decrease of the slope. The degree of the laminarization and enhancement of turbulence on corresponding sides increases with rotation number. These results agree with experimental (Macfarlane and Joubert, 1998) and computational results (Kristoffersen and Andersson, 1993) for a rotating channel. Fig. 8 shows the average friction factor $f = 8\left(\frac{\langle u_\tau \rangle}{u_b}\right)^2$ over the duct perimeter which is normalized by the friction factor for a stationary duct of

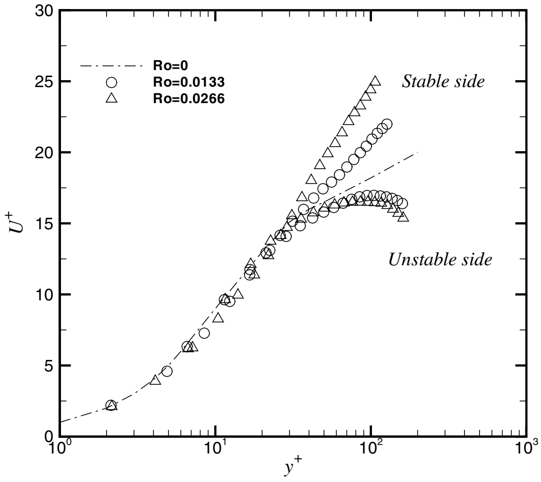

Fig. 7. Streamwise mean velocity along wall bisector $z/D_h = 0.5$.

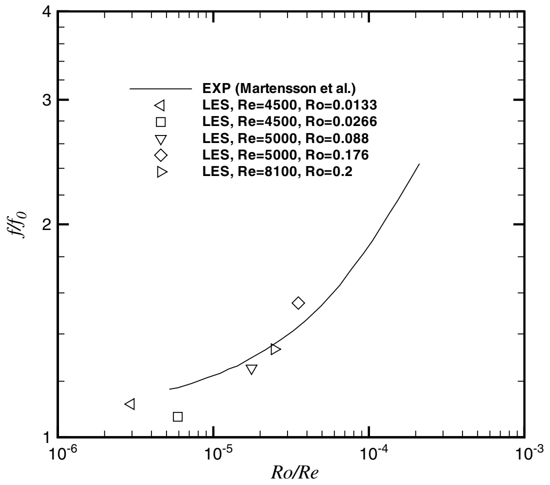

Fig. 8. Average friction factor over duct perimeter.

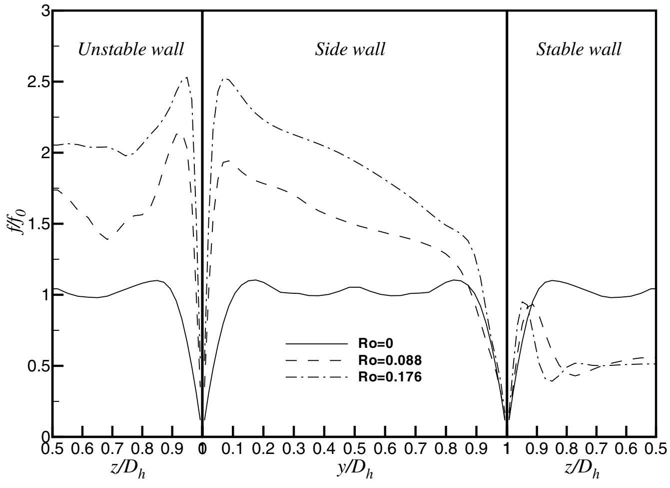

Fig. 9. Local friction factor along duct perimeter.

the same Reynolds number, which is given by Jones' correlation Jones (1976)

$$1/\sqrt{f_0} = 2\log\left(1.125Re\sqrt{f_0}\right) - 0.8. \tag{29}$$

The present LES results (a $Re = 8100$, $Ro = 0.2$ case is also included) are compared with the curve which was obtained by matching the experimental data of Martensson et al. (2002). It can be seen that the friction factor increases rapidly with rotation number. By comparing the local friction velocities along the duct periphery under different rotation numbers, which is shown in Fig. 9, it can be seen that the increase of friction factor mainly takes place on the unstable wall and the side wall. Fig. 10 shows the root mean square (r.m.s.) of velocity fluctuations along the wall

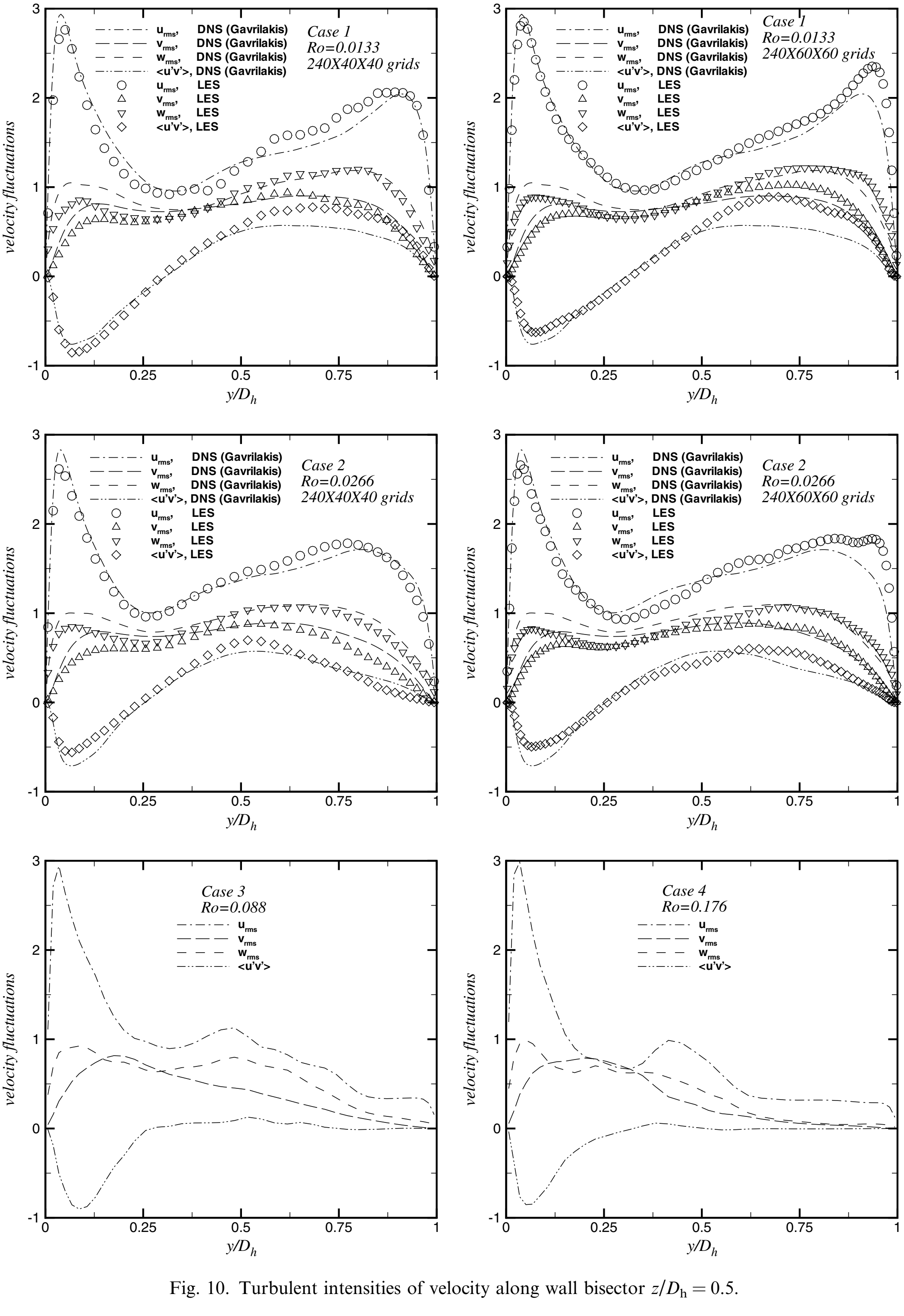

Fig. 10. Turbulent intensities of velocity along wall bisector $z/D_h = 0.5$.

bisector $z/D_\mathrm{h} = 0.5$. These fluctuations are normalized by the global wall friction velocity.

A very interesting phenomenon is, unlike in a rotating channel in which cross-stream fluctuations always show maxima near the unstable wall (see Kristoffersen and Andersson, 1993; Tafti and Vanka, 1991), in a rotating duct cross-stream fluctuations are higher at the stable wall when rotation number is small. This difference can be attributed to the contribution of the secondary flows to the turbulent production in rotating duct, which cannot be ignored as in a rotating channel. The interpretation of the results in Fig. 10 can be facilitated by examining the production terms in the Reynolds stress transport equations:

$$M_{ij} = P_{ij} + G_{ij}, \tag{30}$$

$$P_{ij} = -\rho\left(\langle u_i'u_k'\rangle \frac{\partial U_j}{\partial x_k} + \langle u_j'u_k'\rangle \frac{\partial U_i}{\partial x_k}\right), \tag{31}$$

$$G_{ij} = 2\rho Ro\left(\langle u_i'u_l'\rangle \varepsilon_{jl3} + \langle u_j'u_l'\rangle \varepsilon_{il3}\right), \tag{32}$$

where P_{ij} is caused by mean shear and G_{ij} by rotation. $\langle\cdot\rangle$ represents time averaging. The dominant components of P_{ij} and G_{ij} are shown in Table 2.

M_{11} and u_rms distributions at low and high rotation numbers are shown in Fig. 11. Since $P_{11} \gg G_{11}$ in the current rotation number range, M_{11} is almost the same as P_{11}. Because $\langle u'v'\rangle$ is of opposite sign to $\frac{\mathrm{d}U}{\mathrm{d}y}$ and $\langle u'w'\rangle$ is of opposite sign to $\frac{\mathrm{d}U}{\mathrm{d}w}$, P_{11} is positive. Under low rotation rate, the contribution of $\frac{\mathrm{d}U}{\mathrm{d}w}$ to P_{11}, which causes M_{11} to attain local maximum near the horizontal wall, is of the same order as the contribution of $\frac{\mathrm{d}U}{\mathrm{d}y}$. When the rotation number is high, due to the Taylor–Proudman effect, the contribution of $\frac{\mathrm{d}U}{\mathrm{d}w}$ to P_{11} is negligible. Another feature of the M_{11} distributions is that under low rotation number, there are peak values near both stable and unstable walls while under high rotation number the peak value only appears near the unstable wall. This is because of the vanishing $\langle u'v'\rangle$ at the negative $\frac{\mathrm{d}U}{\mathrm{d}y}$ part under high rotation number. As for $\langle u'v'\rangle$, when the rotation rate is low, P_{12} dominates in M_{12}. At high rotation numbers (such as that in case 4), G_{12} is of the same order of magnitude as P_{12}. Furthermore, in the positive $\frac{\mathrm{d}U}{\mathrm{d}y}$ part, G_{12} is of the same sign as P_{12} while in the negative $\frac{\mathrm{d}U}{\mathrm{d}y}$ part, G_{12} is of opposite sign to P_{12} which causes M_{12} to be small and $\langle u'v'\rangle$ to vanish. These effects are shown in Fig. 12. $\langle v'^2\rangle$ is affected by M_{22} as Fig. 13 shows. At low rotation number, the secondary flow induced P_{22} dominates in M_{22} and results in a higher v_rms near the stable wall. At high rotation number, G_{22} dominates in M_{22} and as a result, v_rms shows only one peak near the unstable wall.

3.2. The heated duct

The domain for the heated rotating duct cases are the same as that of the isothermal cases which is shown in Fig. 1. Heat is applied to all four walls of the test section. The constant wall heat flux condition is employed. As mentioned above, rotation reduces/increases streamwise veloc-

Table 2
Turbulent production terms

ij	11	22	33	12
P_{ij}	$-2\rho(\langle u'v'\rangle \frac{\partial U}{\partial y} + \langle u'w'\rangle \frac{\partial U}{\partial z})$	$-2\rho(\langle v'^2\rangle \frac{\partial V}{\partial y} + \langle v'w'\rangle \frac{\partial V}{\partial z})$	$-2\rho\langle w'^2\rangle \frac{\partial W}{\partial z}$	$-\rho\langle v'^2\rangle \frac{\partial U}{\partial y}$
G_{ij}	$4\rho Ro\langle u'v'\rangle$	$-4\rho Ro\langle u'v'\rangle$	0	$2\rho Ro(\langle v'^2\rangle - \langle u'^2\rangle)$

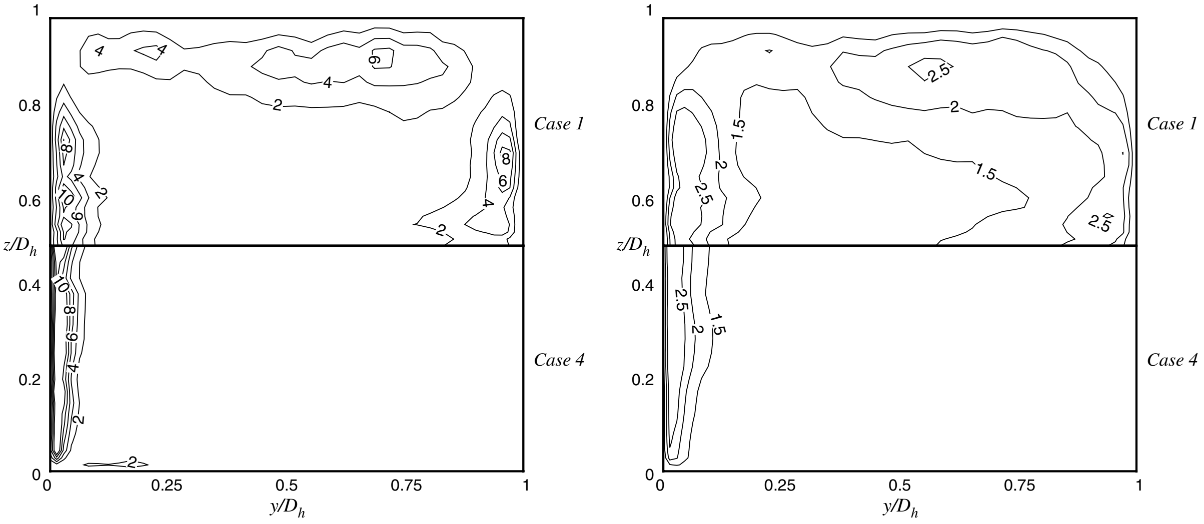

Fig. 11. Contours of M_{11} (left) and u_rms (right).

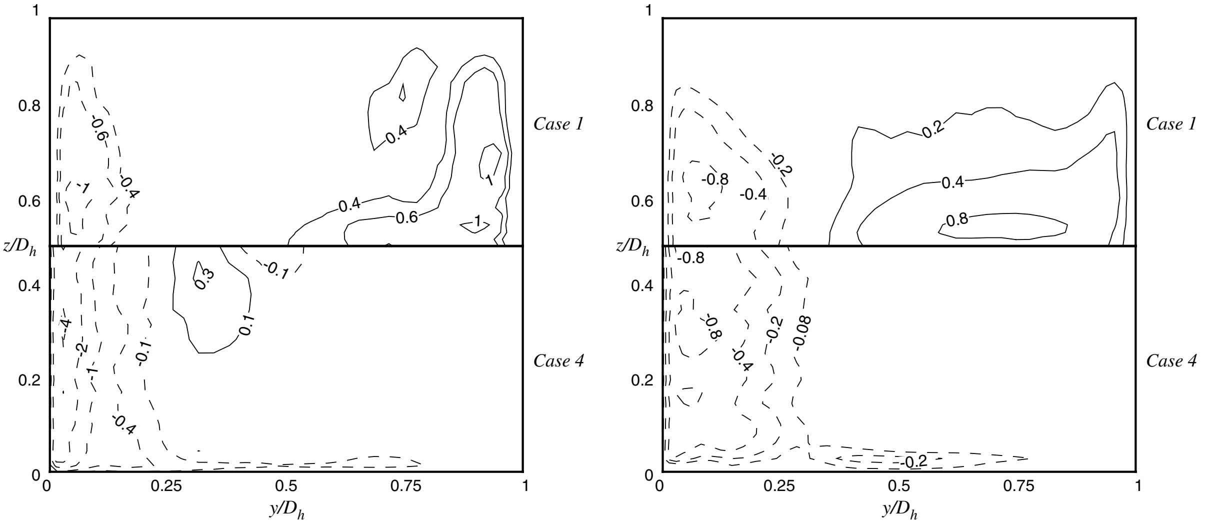

Fig. 12. Contours of M_{12} (left) and $\langle u'v' \rangle$ (right).

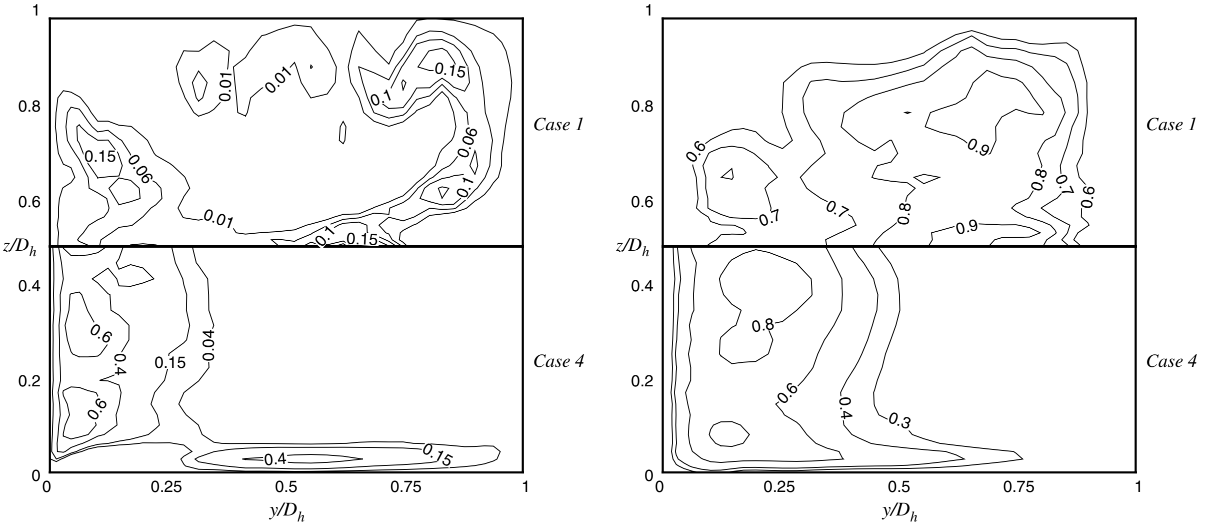

Fig. 13. Contours of M_{22} (left) and v_{rms} (right).

ity at the stable/unstable wall which results in relatively higher/lower local temperature at the stable/unstable wall. Density differences arise as a consequence of this local temperature difference. The buoyancy acts in the aiding/opposing direction to the mean flow at the unstable/stable side, respectively, if the Grashof number is positive (outward flow) and the situation is reversed when the Grashof number is negative (inward flow). In comparison with the buoyancy-free flow, the opposing buoyancy at the stable side in the outward flow causes the streamwise velocity there to decrease and eventually the flow separates under the current Grashof numbers. As a result, a significant temperature rise appears at the stable side near the inlet of the heated section ($x/D_{\mathrm{h}} = 2$). This reduces the Nusselt number on the stable wall. However, further downstream the temperature at the stable wall decreases somewhat. This is due to the enhancement of the near-wall turbulent kinetic energy and the turbulent transport near the stable wall, which causes a slight increase in Nusselt number (see Figs. 14, 17, 18 and 20). For the inward flow, the aiding buoyancy increases the streamwise velocity near the stable side and as a result the temperature/Nusselt number at the stable side is much lower/higher than that of the buoyancy-free flow at the same streamwise location.

These effects can be seen from Fig. 14 which presents mean streamwise velocity and temperature profiles at the wall bisector $z/D_{\mathrm{h}} = 0.5$ for forced and mixed convection cases.

The cross section distributions of the mean velocity (contours of U^+ and vectors of secondary flow) and temperature θ at station $x/D_{\mathrm{h}} = 10$ are shown in Fig. 15. Here the non-dimensional temperature is defined as $\theta = \frac{T - \langle T_{\mathrm{w}} \rangle}{\langle T_{\tau} \rangle}$, where $\langle T_{\mathrm{w}} \rangle$ is the average wall temperature and $\langle T_{\tau} \rangle$ is the average friction temperature. It can be seen that

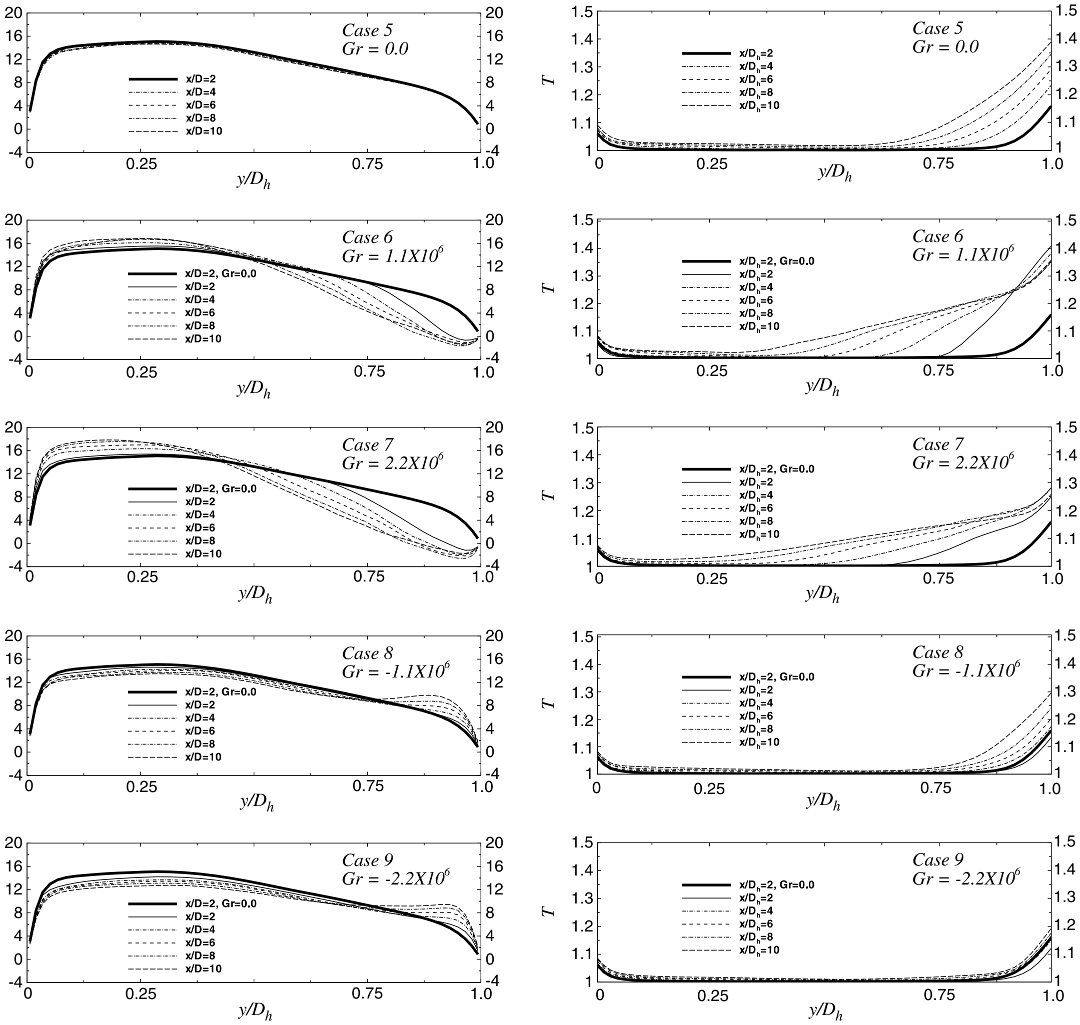

Fig. 14. Streamwise mean velocity and temperature along wall bisector $z/D_h = 0.5$.

compared with the buoyancy-free flow, the secondary flow patterns become more complex because of buoyancy. In the outward mixed flows, the small rotating cell at the unstable side is suppressed and the large rotating cell near the stable side is also weakened in strength and moved toward the unstable side. In the inward mixed flows, the small rotating cell does not change much compared with forced flow and the large rotating cell is strengthened. At high Grashof number (case 9), a new cell appears near the center of the stable wall in the inward flow. These secondary flow pattern changes have significant impacts on the streamwise velocity and temperature distributions which can be most obviously observed in the inward flows where streamwise velocity isolines are severely distorted from the original Taylor–Proudman regime.

These phenomena can be explained by the force balance mentioned above. As Fig. 15 shows (where P means pressure gradient, C means Coriolis force), in the outward flows, the flow separation near the stable side causes the Coriolis force to reverse direction which promotes a pressure gradient toward the unstable wall. This adverse pressure gradient does not favor the development of the Ekman layer at the side wall. As a result, the impingement of fluid from the Ekman layer toward the stable wall is impaired. The rotating cell at the corner is then weakened and shifted toward the unstable side. In the inward flows, on the contrary, the aiding buoyancy at the stable side accelerates the local streamwise velocity and results in increased Coriolis force and pressure gradient. This enhanced favorable pressure gradient helps the development of the Ekman layer as well as the flow impingement toward the stable wall. Thus, the corner vortex is strengthened.

The variations of the secondary flow pattern affect the temperature and Nusselt number distributions at the stable wall as follows. The Stewartson layer transports hot fluid from the stable wall to the duct interior and the Ekman layer transports cold fluid from the duct center to the stable wall corner. Thus in the buoyancy-free flows, the temperature peak appears at the center of stable wall and the Nusselt number maximum shows up at the corner. In the outward flows, the Ekman layer is hindered as analyzed

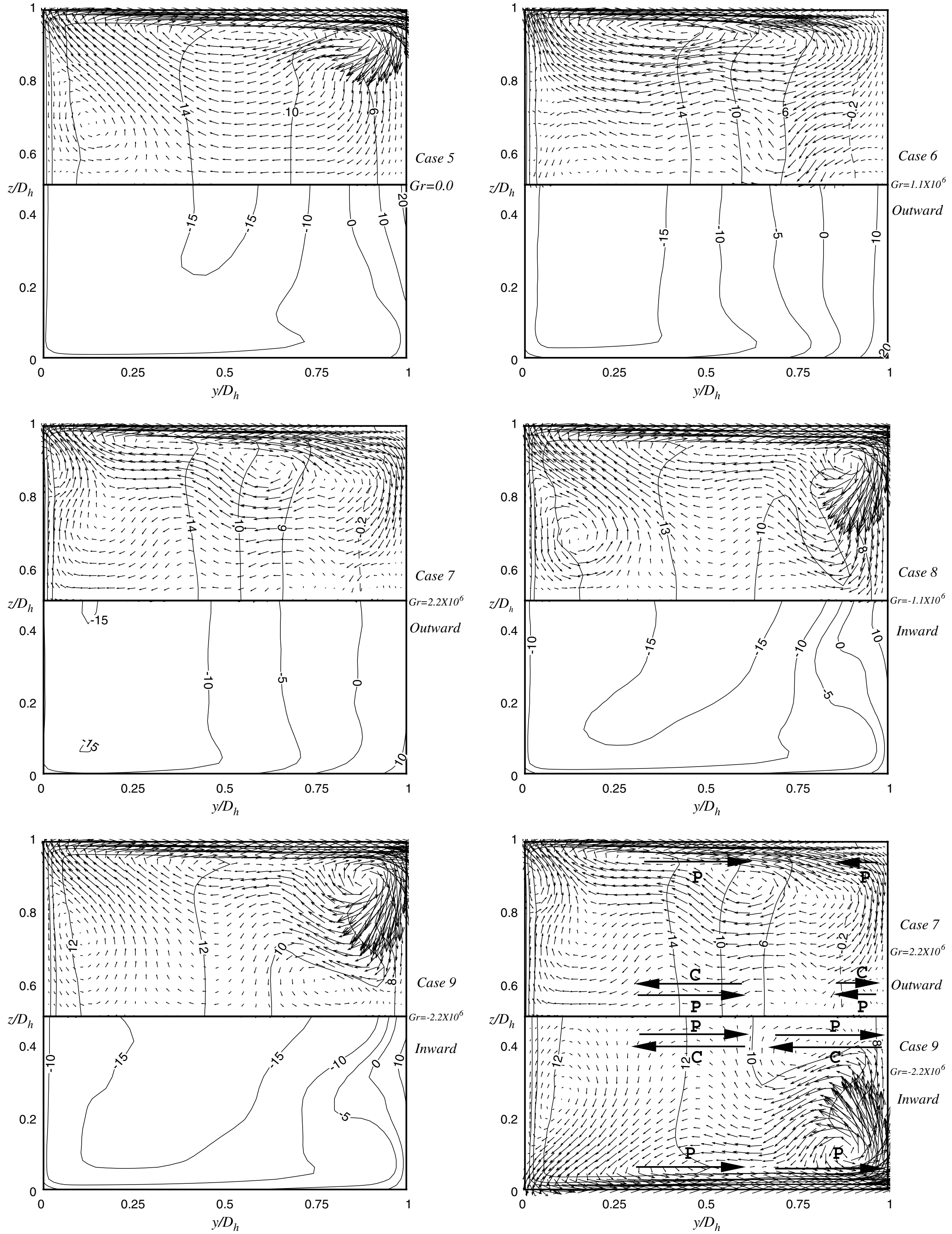

Fig. 15. Mean velocity (up) and temperature (below) at $x/D_\mathrm{h} = 10$ and schematic of the mechanism of the variations of secondary flows.

above; therefore, the temperature peak on the stable wall shifts to the corner and the Nusselt number maximum shows up near the stable wall-bisector. In the inward flows, the Ekman layer is strengthened. As a result, the impingement of cold fluid toward the stable wall corner is also strengthened; therefore, the temperature peak on the stable wall is located near the wall-bisector. In the case of Grashof number -2.2×10^6, a new rotating cell appeared near the stable wall center and it also transports relatively cold fluid toward the stable wall, which is responsible for the shift of the local stable wall temperature maximum from the wall bisector toward the corner.

The local temperature and Nusselt number distributions along the duct perimeter are shown in Figs. 16 and 21,

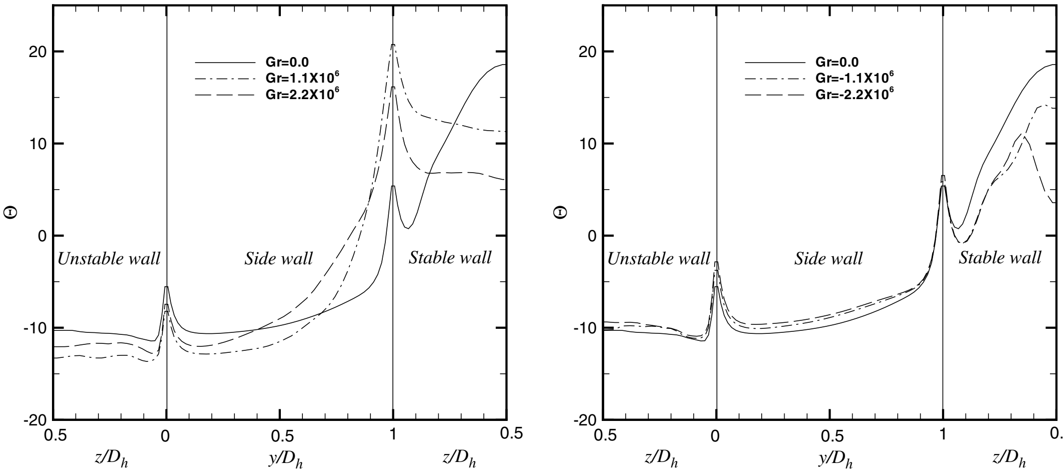

Fig. 16. Local temperature distributions along duct perimeter at $x/D_\mathrm{h} = 10$.

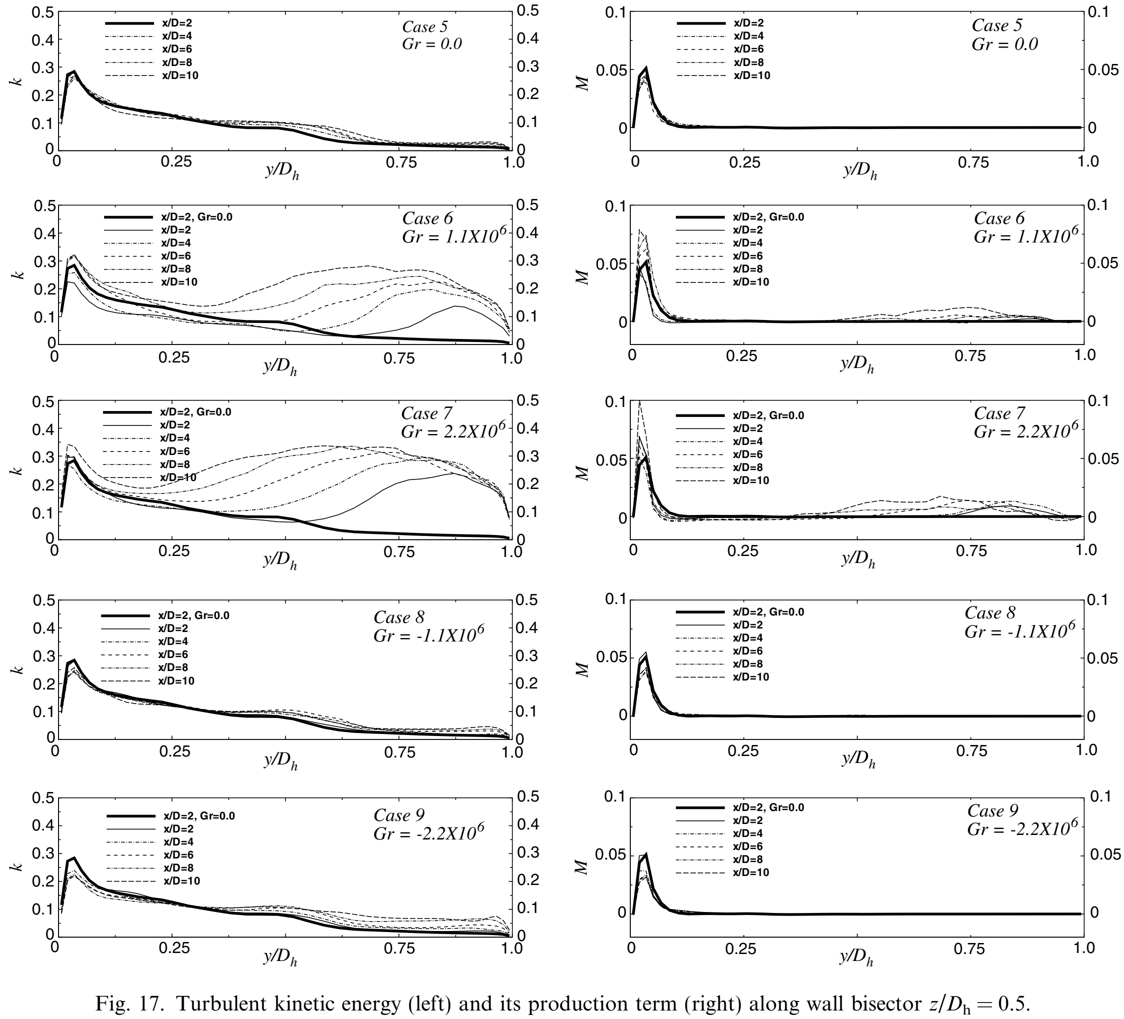

Fig. 17. Turbulent kinetic energy (left) and its production term (right) along wall bisector $z/D_\mathrm{h} = 0.5$.

respectively, in which the phenomena mentioned above can be observed.

The variations of the secondary flow pattern also influence the mean shear stress distribution on the stable wall. Since the Ekman layer transports high speed fluid from the duct interior to the stable wall and the Stewartson layer transports low speed fluid from the stable side to the duct interior, in the buoyancy-free flows, the mean shear stress on the stable wall obtains its peak value at the corner. In the inward flows, the strengthened secondary flow results in high temperature near the central stable wall as mentioned above. And the aiding buoyancy accelerates the hot fluid; thus, a high shear stress appears near the central stable wall in the inward flows.

In summary, rotation causes the streamwise velocity to increase/decrease near the unstable/stable side. The different balances between Coriolis force, pressure gradient and viscous force give rise to persistent secondary flow patterns. Under heating the streamwise velocity differences cause temperature differences (and as a result, density differences) across the duct. The buoyancy effects due to these density differences change streamwise velocity distributions and through the force balance change the secondary flow patterns. The modified velocity field changes the temperature field through convection and the modified temperature field in turn affects velocity field through buoyancy force. At the same time, the velocity and temperature fluctuations are also influenced by buoyancy.

The turbulent kinetic energy $k = \frac{1}{2}\langle u_i' u_i' \rangle$ distributions and the production term of the Reynolds averaged TKE (turbulent kinetic energy) equation at the wall bisector $z/D_\mathrm{h} = 0.5$ are shown in Fig. 17. The production term M is composed of two parts: P, the production due to mean shear and G, production due to buoyancy. These terms are given in the following equation:

$$M = P + G, \tag{33}$$

$$P = -\rho \langle u_i' u_k' \rangle \frac{\partial U_i}{\partial x_k}, \tag{34}$$

$$G = \frac{Gr}{\varepsilon Re_\mathrm{r}^2} \langle \rho' u' \rangle. \tag{35}$$

Coriolis force makes no contribution to the turbulent energy production term. The production term P also can be divided into two parts:

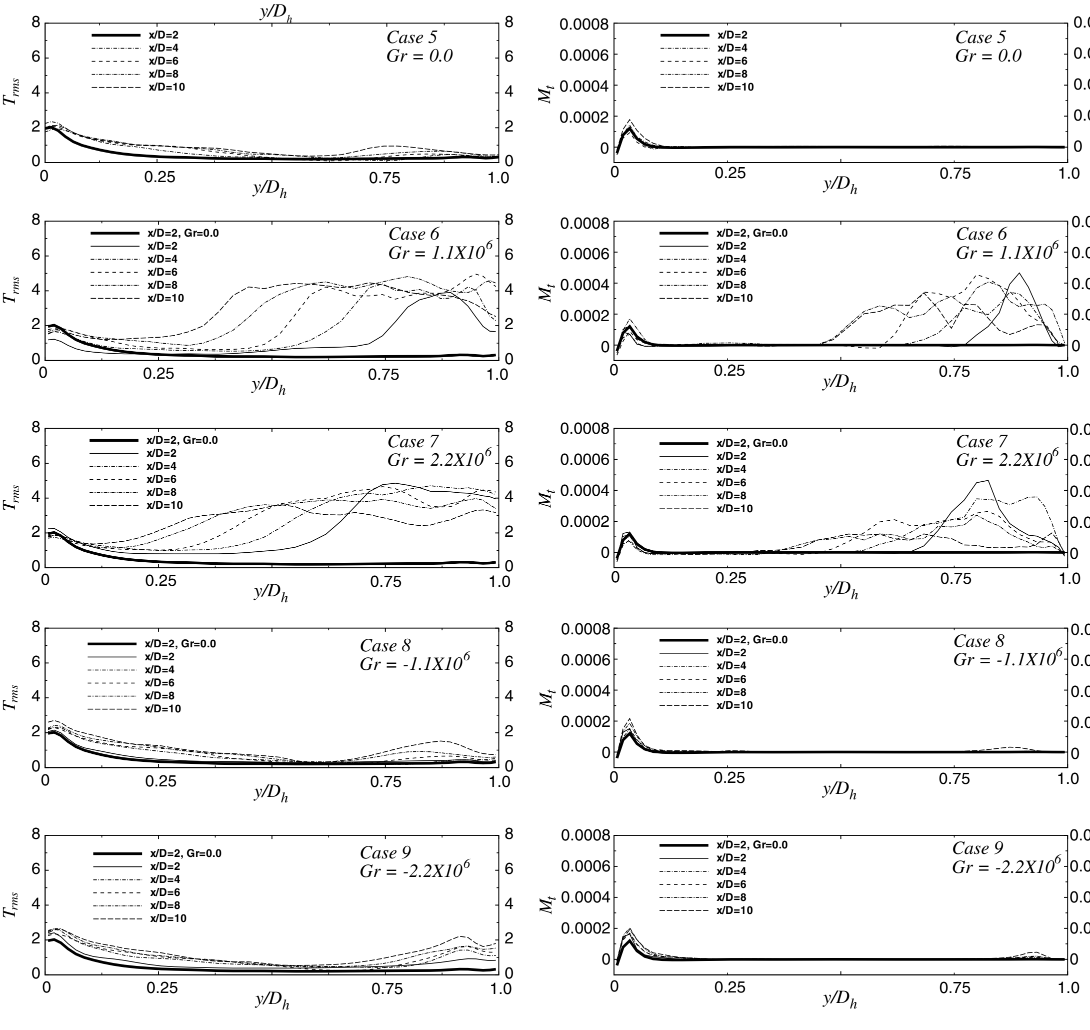

Fig. 18. Temperature fluctuation intensity (left) and its production term (right) along wall bisector $z/D_\mathrm{h} = 0.5$.

$$P = P_{\text{accel}} + P_{\text{shear}}, \tag{36}$$

$$P_{\text{accel}} = -\rho\left(\langle u'^2\rangle\frac{\partial U}{\partial x} + \langle v'^2\rangle\frac{\partial V}{\partial y} + \langle w'^2\rangle\frac{\partial W}{\partial z}\right). \tag{37}$$

The first part is the TKE absorption rate caused by mean flow acceleration and the second part is the terms determined by shear stress. The TKE absorption rate is always negative when the flow is under heating. The reason is that the density of the fluid keeps decreasing under heating, so the velocity of the flow keeps increasing so that a constant mass flow rate can be maintained. In the present study, P_{shear} dominates the production term. The production term caused by buoyancy, though only about 10% of the total production currently, can dominate when the buoyancy parameter $\frac{Gr}{\varepsilon Re_{\text{r}}^2}$ becomes larger. In the outward flows, P_{shear} increases near the stable side because of the strong shear gradient caused by the flow separation. In contrast, in the inward flow, P_{shear} decreases slightly near the unstable side because of the reduced shear gradient.

The temperature fluctuation intensities T_{rms} and their production term along the wall bisector $z/D_{\text{h}} = 0.5$ are shown in Fig. 18. The production term M_{t} is given by

$$M_{\text{t}} = -\rho\langle u_i'T'\rangle\frac{\partial T}{\partial x_i}. \tag{38}$$

Unlike in the thermally fully-developed flows, the contribution from the streamwise turbulent heat flux and temperature gradient, $-\rho\langle u'T'\rangle\frac{\partial T}{\partial x}$ together with the contribution from the vertical components $-\rho\langle v'T'\rangle\frac{\partial T}{\partial y}$ dominates the production term in the present developing heat transfer situations. It can be seen that the temperature fluctuations, like turbulent kinetic energy, are suppressed near the stable side in the forced flow. This is due to the distributions of the turbulent heat flux components, which are also suppressed near the stable side. In the outward mixed flows, the temperature fluctuations are markedly higher than that of forced flow near the stable side which is due to the enhanced streamwise and vertical components of turbulent

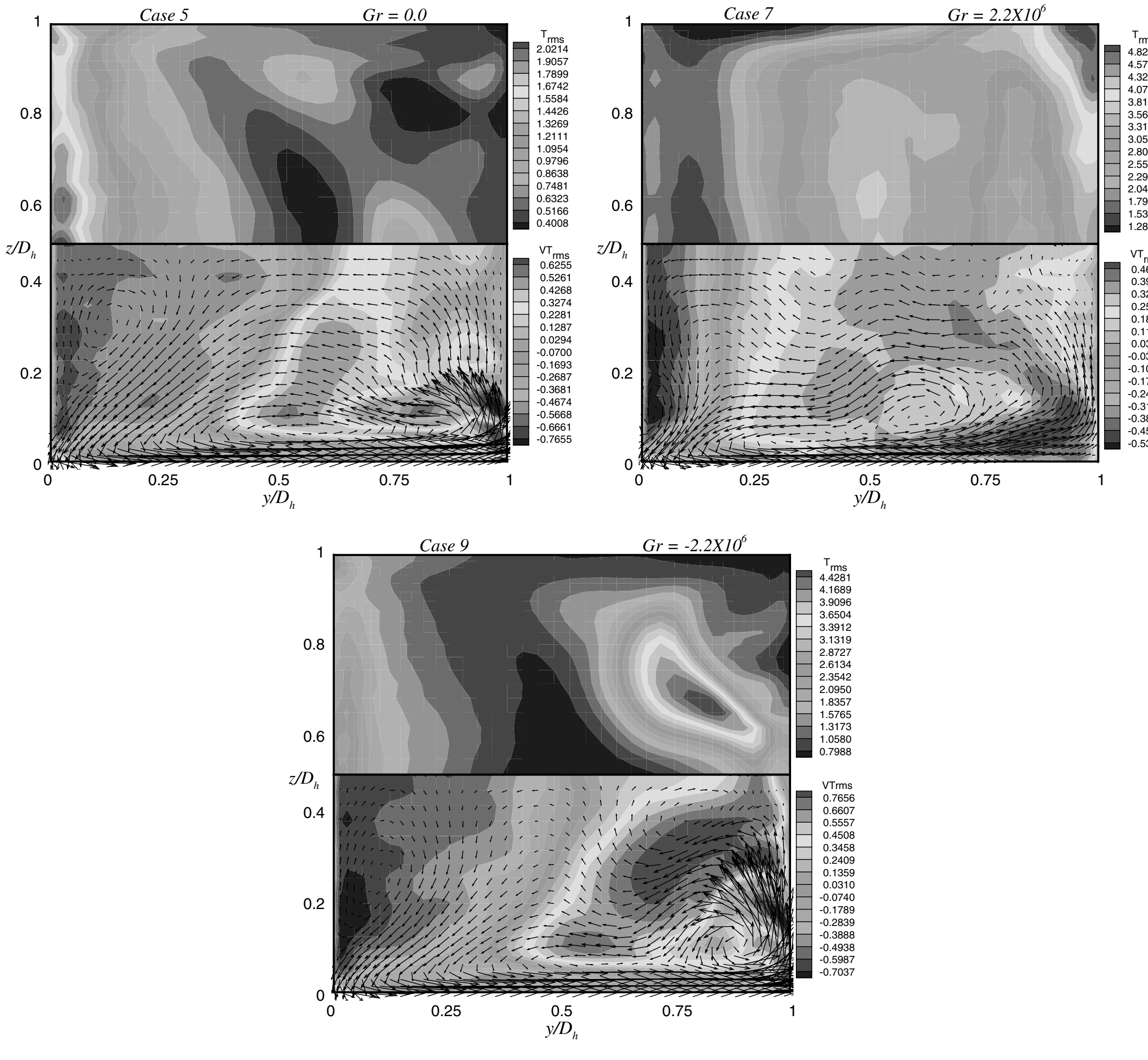

Fig. 19. Temperature fluctuation intensity (up) and vertical turbulent heat flux (below) at $x/D_{\text{h}} = 10$.

heat flux as a result of the augmented mixing. This helps to compensate for the effect of mean flow separation which reduces the Nusselt number near the stable wall. In the inward mixed flows, the temperature fluctuations increase near the stable side which can be attributed to the strengthening of the corner rotating cell. To aid in understanding the relation of secondary flows to the temperature fluctuations, the distributions of temperature fluctuation and the vertical component of turbulent heat flux $-\langle v'T'\rangle$ together with the secondary flow vectors in the cross section are shown in Fig. 19. These results were obtained at the location $x/D_{\mathrm{h}} = 10$. A very strong relation between secondary flows and the vertical component of turbulent heat flux can be observed. A negative $-\langle v'T'\rangle$ zone appears near the unstable wall and a positive $-\langle v'T'\rangle$ zone appears near the stable wall. The size of the negative $-\langle v'T'\rangle$ zone is controlled by the size of the small rotating cell near the unstable side. In the outward mixed flow, the small rotating cell is suppressed which results in the reduction of this zone. The positive $-\langle v'T'\rangle$ zone is related to the large rotating cell near the stable side. In the outward mixed flow, the large rotating cell and the positive $-\langle v'T'\rangle$ zone are both displaced towards the unstable side. In the inward mixed flow, the strengthened stable side rotating cell causes an intensified positive $-\langle v'T'\rangle$ zone, which is responsible for the augmentation of temperature fluctuations near the stable side compared with the forced flow.

The streamwise distribution of the wall-averaged Nusselt number ratio Nu_x/Nu_{s} is shown in Fig. 20. The Reynolds number and the rotation number are fixed at $Re = 5000$ and $Ro = 0.176$, respectively. Nu_x is the local peripherally averaged Nusselt number. The reference Nusselt number Nu_{s} is the fully developed Nusselt number for stationary straight pipe flow correlated by Dittus–Boelter/McAdams as $Nu_{\mathrm{s}} = 0.023Re^{0.8}Pr^{0.4}$. The triangles are the experimental data of Han and Zhang (1992). Compared with buoyancy-free flow, the heat transfer coefficient is enhanced at the unstable wall in the outward mixed flows as well as the stable wall in the inward mixed flows due to the increased mean shear, which is caused by the aiding buoyancy. The opposing buoyancy near the stable side in the outward mixed flows causes the flow to separate. The slow speed flow close to the stable wall reduces the Nusselt number at first; however, as the flow goes downstream, the situation is improved because of the enhanced turbulent kinetic energy near the stable side. As can be observed, the stable wall Nusselt number of the $Gr = 2.2 \times 10^6$ case surpasses the $Gr = 1.1 \times 10^6$ case at $x/D_{\mathrm{h}} = 1.4$ and then surpasses the forced flow at $x/D_{\mathrm{h}} = 8$. The Nusselt numbers at the side wall of the outward mixed flows are lower than that of the forced flow. The four-wall averaged Nusselt number of the outward mixed flow is lower than that of the forced flow at first but eventually becomes higher than the forced flow. For the inward mixed flows, the unstable wall Nusselt number is less than that of the forced flow because the opposing buoyancy retards the streamwise mean velocity near the unstable side. However, in the current developing situation, there is no obvious differences in the side wall and four-wall averaged Nusselt number between the inward mixed and forced flow.

The local Nusselt number ratio Nu/Nu_{s} and mean shear stress τ/τ^{a} distribution along the duct perimeter at $x/D_{\mathrm{h}} = 10$ are shown in Fig. 21. Here τ is obtained by calculating the value of $\mu\frac{U}{\delta}$ of the nearest point from the wall (δ is the distance from the wall) and τ^{a} is the peripherally averaged shear stress. Note that the negative shear stress at the side wall near $y/D_{\mathrm{h}} = 1$ and the stable wall in the outward mixed flows are due to the mean streamwise velocity reversal. A strong correlation between the two distributions can be found, especially near the unstable wall and side

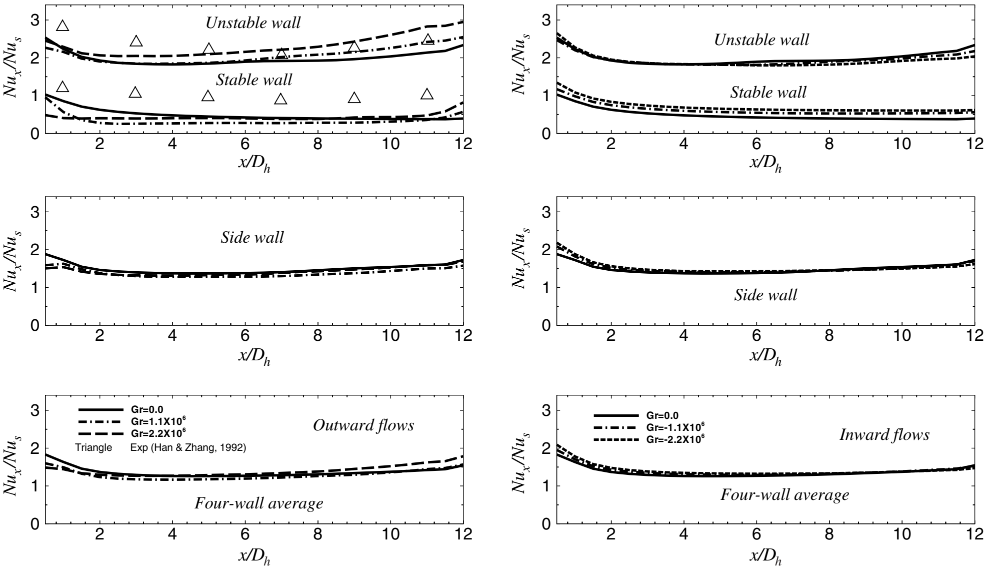

Fig. 20. Streamwise distribution of wall-averaged Nusselt number.

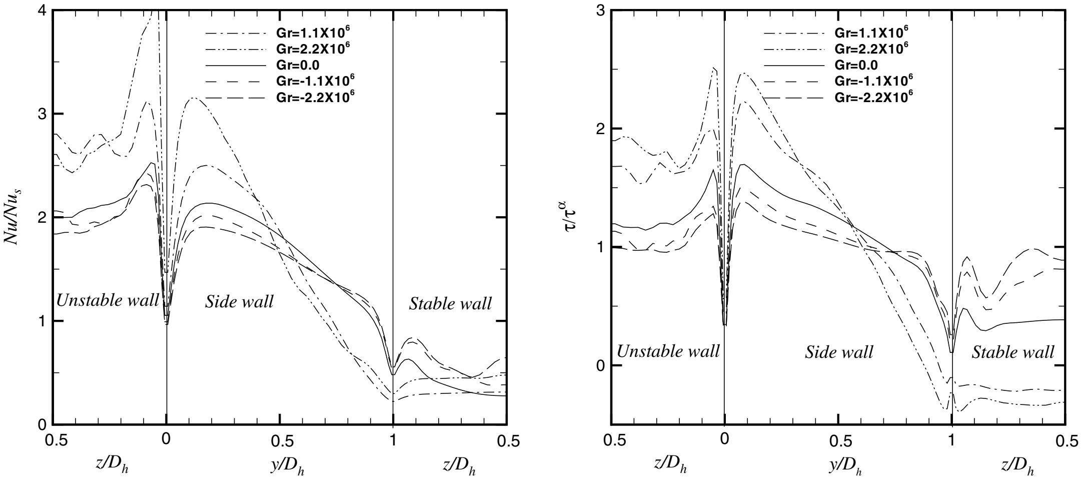

Fig. 21. Local Nusselt number (left) and shear stress (right) along the duct perimeter at $x/D_h = 10$.

wall. At the stable wall, turbulent transport is also important in addition to the mean shear for the outward mixed flows as mentioned.

Attention is now turned to the effects of rotation number and Reynolds number on heat transfer. As shown in Fig. 22, at the same Reynolds number and Grashof number, the differences between the heat transfer coefficients on the unstable and stable walls increase with increasing rotation number; at the same rotation number and Grashof number, the Reynolds number shows little impact on local heat transfer coefficients, which agrees well with the physical meaning of rotation number (which is the measurement of the relative strength of Coriolis force to inertia force) and experimental results (Han and Zhang, 1992).

4. Summary and conclusions

Turbulent mixed convection heat transfer in a variable-property thermally developing rotating square duct was investigated using large eddy simulation. The effects of Coriolis force and rotational buoyancy on the mean flow structure, turbulent fluctuation intensities and heat transfer behavior were studied. Fairly satisfactory agreement between prediction and experimental results has been achieved. The discrepancy may be due to the uncertainty of measurements in experiments (up to 20–25% according to Han and Zhang (1992)) and the boundary condition differences between experiments and simulations. Based on the analysis of the present LES results, the following conclusions can be drawn:

(1) In the fully developed isothermal rotating duct flows, the cross-stream fluctuations ($\langle v'^2\rangle$ and $\langle w'^2\rangle$) obtain their peak values near the stable side rather than near the unstable side when the rotation number is small. This is due to the contribution of secondary flows on the turbulent production.

(2) Buoyancy changes the secondary flow pattern through a delicate force balance. In the outward flows, the opposing buoyancy retards or even reverses the flow near the stable side. This results in a reduced or even reversed Coriolis force and in turn, a reduced

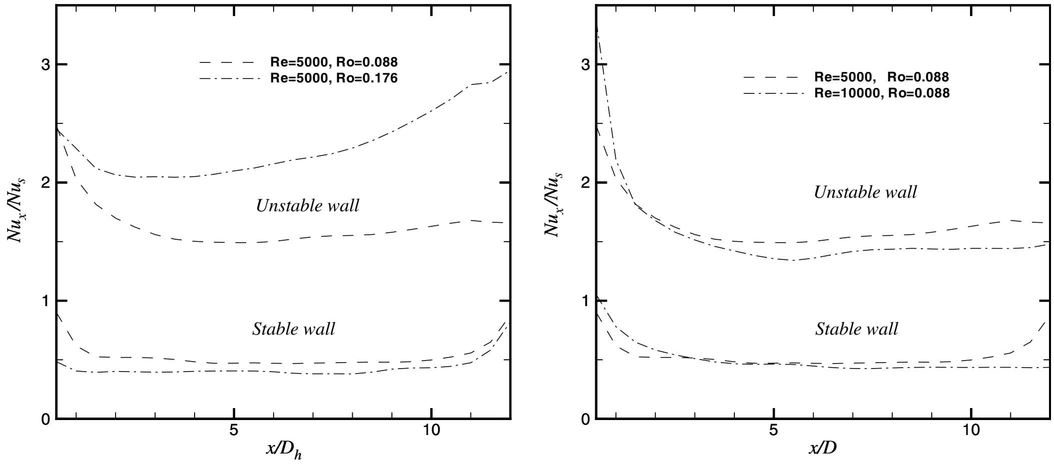

Fig. 22. Streamwise distribution of wall-averaged Nusselt number at different rotation and Reynolds numbers.

favorable or even adverse pressure gradient which does not favor the development of the Ekman layer at the side wall and, as a result, weakens the stable wall corner rotating cell. In the inward flows, the aiding buoyancy accelerates fluids close to the stable wall giving rise to an enhanced favorable pressure gradient which strengthens the Ekman layer as well as the stable wall corner rotating cell.

(3) Buoyancy influences the temperature (and as a result, Nusselt number) and mean shear stress distribution on the stable wall not only by changing the streamwise velocity directly, but also by modifying secondary flow patterns. Since the Ekman layer transports cold and high speed fluid from the duct interior to the stable wall and the Stewartson layer transports hot and low speed fluid from the stable side to the duct interior, in the buoyancy-free flows, the Nusselt number and mean shear stress on the stable wall obtains their peak values at the corner, while the temperature maximum appears at the wall-bisector. In the outward flows, the weakened secondary flow results in high temperature near the stable side corner and a Nusselt number maximum at the wall-bisector. In the inward flows, the strengthened secondary flow results in high temperature near the central stable wall. The aiding buoyancy accelerates the hot fluid; thus, a high shear stress appears near the stable wall-bisector in the inward flows. This explains the discrepancy between the Nusselt number and shear stress distributions at the stable wall.

(4) Buoyancy affects turbulent kinetic energy and temperature fluctuation distributions through its contributions to the relevant production terms. Buoyancy influences the production of turbulent kinetic energy in two ways: by modifying the mean shear and by acting directly as a buoyancy production term. The latter can dominate if the buoyancy parameter $\frac{Gr}{\varepsilon Re_{\mathrm{r}}^{2}}$ becomes large. It has been found that the secondary flow pattern has a strong relationship with the vertical heat flux $-\langle v'T'\rangle$, which is vital in the production term of the temperature fluctuations. Buoyancy thus impacts the temperature fluctuation indirectly by altering the secondary flow pattern.

(5) There is a strong correlation between the peripheral distributions of local Nusselt number and mean shear stress at the unstable wall and the side wall. The discrepancy between the Nusselt number and shear stress distributions at the stable wall is explained in conclusion (3).

Acknowledgements

This research was partially supported by the Air Force Office of Scientific Research under grant F49620-01-1-0113 and by the National Science Foundation under grant CTS-9806989. The computer resources provided by the Iowa State High Performance Computing Center and the Minnesota Supercomputing Institute are gratefully acknowledged. The comments of the reviewers are very helpful and highly appreciated.

References

Belhoucine, L., Deville, M., Elazehari, A.R., Bensalah, M.O., 2004. Explicit algebraic Reynolds stress model of incompressible turbulent flow in rotating square duct. Comput. Fluids 33, 179–199.

Dutta, S., Anderson, M., Han, J.C., 1996. Prediction of turbulent heat transfer in rotating smooth square ducts. Int. J. Heat Mass Transfer 39, 2505–2514.

Gavrilakis, S., private communication. Direct numerical simulation of turbulent flow in rotating straight square duct using spectral methods.

Greitzer, E.M., Tan, C.S., Graf, M.B., 2004. Internal Flow, Cambridge.

Han, J.-C., Zhang, Y.M., 1992. Effect of uneven wall temperature on local heat transfer in a rotating square channel with smooth walls and radial outward flow. J. Heat Transfer 114, 850–858.

Han, J.-C., Zhang, Y.M., Kalkuehler, K., 1993. Uneven wall temperature effect on local heat transfer in a rotating two-pass square channel with smooth walls. J. Heat Transfer 115, 912–920.

Hwang, J.J., Lia, T.Y., Chen, S.H., 1998. Prediction of turbulent fluid flow and heat transfer in a rotating periodical two-pass square duct. Int. J. Numer. Meth. Heat Fluid Flow 8, 519–538.

Jones, O.C., 1976. An improvement in the calculation of turbulent friction in rectangular ducts. J. Fluid Eng. 98, 173–181.

Kim, J.W., Lee, D.J., 2000. Generalized characteristic boundary conditions for computational aeroacoustics. AIAA J. 38, 2040–2049.

Kim, J.W., Lee, D.J., 2004. Generalized characteristic boundary conditions for computational aeroacoustics, part 2. AIAA J. 42, 47–55.

Kristoffersen, R., Andersson, H.I., 1993. Direct simulations of low-Reynolds-number turbulent flow in a rotating channel. J. Fluid Mech. 256, 163–197.

Lin, Y.-L., Shih, T.I.-P., Stephens, M.A., Chyu, M.K., 2001. A numerical study of flow and heat transfer in a smooth and ribbed U-duct with and without rotation. J. Heat Transfer 123, 219–232.

Liou, T.-M., Chen, C.-C., Chen, M.-Y., 2001. TLCT and LDV measurements of heat transfer and fluid flow in a rotating sharp turning duct. Int. J. Heat Mass Transfer 44, 1777–1787.

Liou, T.-M., Chen, C.-C., Chen, M.-Y., 2003. Rotating effect on fluid flow in two smooth ducts connected by a 180-degree bend. J. Fluid Eng. 125, 138–148.

Macfarlane, I., Joubert, P.N., 1998. Effects of secondary flows on developing, turbulent, rotating boundary layers. Exp. Therm. Fluid Sci. 17, 79–89.

Martensson, G.E., Gunnarsson, J., Johansson, A.V., Moberg, H., 2002. Experimental investigation of a rapidly rotating turbulent duct flow. Exp. Fluids 33, 482–487.

Morris, W.D., Ghavami-Nasr, G., 1991. Heat transfer measurements in rectangular channels with orthogonal mode rotation. J. Turbomach. 113, 339–345.

Murata, A., Mochizuki, S., 1999. Effect of cross-sectional aspect ratio on turbulent heat transfer in an orthogonally rotating rectangular smooth duct. Int. J. Heat Mass Transfer 42, 3803–3814.

Murata, A., Mochizuki, S., 2001. Effect of centrifugal buoyancy on turbulent heat transfer in an orthogonally rotating square duct with transverse or angled rib turbulators. Int. J. Heat Mass Transfer 44, 2739–2750.

Murata, A., Mochizuki, S., 2004. Centrifugal buoyancy effect on turbulent heat transfer in a rotating two-pass smooth square channel with sharp 180-deg turns. Int. J. Heat Mass Transfer 47, 3215–3231.

Ovchinnikov, O.N., Rukolaine, A.V., 1985. Initial section in a square duct rotating about the transverse axis. Mekhanika Zhidkosti i Gaza 5, 41–46.

Pallares, J., Davidson, L., 2000. Large-eddy simulations of turbulent flow in a rotating square duct. Phys. Fluids 12, 2878–2894.

Pallares, J., Davidson, L., 2002. Large-eddy simulations of turbulent heat transfer in stationary and rotating square ducts. Phys. Fluids 14, 2804–2816.

Piomelli, U., Liu, J., 1995. Large eddy simulation of rotating channel flows using a localized dynamic model. Phys. Fluids 7, 839–848.

Pletcher, R.H., Chen, K.-H., 1993. On solving the compressible Navier–Stokes equations for unsteady flows at very low Mach numbers. AIAA Paper 93-3368.

Poinsot, T.J., Lele, S.K., 1992. Boundary conditions for direct simulations of compressible viscous flow. J. Comput. Phys. 101, 104–129.

Prakash, C., Zerkle, R., 1992. Prediction of turbulent flow and heat transfer in a radially rotating square duct. J. Turbomach. 114, 835–846.

Qin, Z.H., Pletcher, R.H., 2004. Large eddy simulation of turbulent heat transfer in a square duct. In: Proceedings of 2004 ASME International Mechanical Engineering Congress and RD&D Expo, Anaheim, USA.

Rieger, H., Jameson, A., 1988. Solution of steady three dimensional compressible Euler and Navier–Stokes equations by an implicit LU scheme. AIAA Paper 88-0619.

Rudy, D.H., Strikwerda, J.C., 1981. Boundary conditions for subsonic compressible Navier–Stokes calculations. Comput. Fluids 9, 327–338.

Smirnov, E.M., 1978. Asymptotic drag formulas for rapidly rotating radial channels of rectangular cross section. Mekhanika Zhidkosti i Gaza 6, 42–49.

Stewartson, K., 1957. On almost rigid rotations. J. Fluid Mech. 3, 17–26.

Tafti, D.K., Vanka, S.P., 1991. A numerical study of the effects of spanwise rotation on turbulent channel flow. Phys. Fluids 3, 642–656.

Tekriwal, P., 1994. Heat transfer predictions with extended k-ε turbulence model in radial cooling ducts rotating in orthogonal mode. J. Heat Transfer 116, 369–380.

Thompson, K.W., 1987. Time dependent boundary conditions for hyperbolic systems. No. 1. J. Comput. Phys. 68, 1–24.

Thompson, K.W., 1990. Time dependent boundary conditions for hyperbolic systems. No. 2. J. Comput. Phys. 89, 439–461.

Vreman, B., Geurts, B., Kuerten, H., 1995. Subgrid-modeling in LES of compressible flow. Appl. Sci. Res. 54, 191–203.

Wagner, J.H., Johnson, B.V., Hajek, T.J., 1991. Heat transfer in rotating passages with smooth walls and radial outward flow. J. Turbomach. 113, 42–51.

Wang, W.-P., Pletcher, R.H., 1996. On the large eddy simulation of a turbulent channel flow with significant heat transfer. Phys. Fluids 8, 3354–3366.

Wang, X.H., Pletcher, R.H., 2005. Large eddy simulation of supercritical CO_2 pipe flow with constant wall heat flux. In: Proceedings of 35th AIAA Fluid Dynamics Conference and Exhibit, Toronto, Canada.